# Integrative proteomics and lipidomics reveals dual roles for lipid droplets in the host cell antiviral response

**Karla helbig**

k.helbig@latrobe.edu.au

School of Agriculture, Biomedicine and Environmnet, La Trobe University https://orcid.org/0000-0001-6306-2821

**Ebony Monson**

La Trobe University https://orcid.org/0000-0001-5632-9575

**Zahra Telikani**

La Trobe University

**Jay Laws**

La Trobe University

**Abbey Milligan**

La Trobe University

**Ashley Rozario**

La Trobe University

**Irumi Amarasinghe**

La Trobe University

**Monique Smith**

University of Melbourne

**Sarah Bamford**

La Trobe University

**Vivian Tran**

La Trobe University

**Quynh Dinh**

La Trobe University

**Nicholas Williamson**

Melbourne Mass Spectrometry and Proteomics Facility https://orcid.org/0000-0002-2173-3452

**Adam Mechler**

La Trobe University https://orcid.org/0000-0002-6428-6760

**Paul Pigram**

La Trobe University https://orcid.org/0000-0002-7972-492X

**Jessica Holien**
RMIT University
**Chad Johnson**
Monash University https://orcid.org/0000-0002-9304-5448
**Shuai Nie**
University of Melbourne
**Markus Hofer**
University of Sydney https://orcid.org/0000-0001-5111-3978
**Donna Whelan**
School of Molecular Sciences, La Trobe University

---

**Article**

**Keywords:** lipid droplets, virus, RNA, lipidomics, proteomics, dual omics, signalling, antiviral, innate immunity

**Posted Date:** July 10th, 2025

**DOI:** https://doi.org/10.21203/rs.3.rs-7006641/v1



**Additional Declarations:** There is **NO** Competing Interest.

---

# Integrative proteomics and lipidomics reveals dual roles for lipid droplets in the host cell antiviral response.

EA Monson[1,2†*], Z Telikani[1,2†], JL Laws[1,2†], AJ Milligan[2,3], AM Rozario[2,3], I Amarasinghe[1,2], ML Smith[1,2], SE Bamford[4], V Tran[1,2,5], QN Dinh[1,2,5], N Williamson[6], A Mechler[7,2], PJ Pigram[4], JK Holien[8,9,10], CJ Johnson[11], S Nie[6], MJ Hofer[12], DR Whelan[2,3] and KJ Helbig[1,2*].

**Affiliations:**

[1] Department of Microbiology, Anatomy, Physiology and Pharmacology, La Trobe University, Bundoora, Victoria, Australia

[2] La Trobe Institute for Molecular Science, La Trobe University, Bundoora, Victoria, Australia

[3] Holsworth Biomedical Research Centre, La Trobe University, Bendigo, Australia.

[4] Centre for Materials and Surface Science and Department of Mathematical and Physical Sciences, La Trobe University, Bundoora, Victoria, Australia

[5] Centre for Cardiovascular Biology and Disease Research, La Trobe Institute for Molecular Science

[6] Melbourne Mass Spectrometry and Proteomics Facility, Bio21 Molecular Science & Biotechnology Institute, The University of Melbourne, Melbourne, Victoria, Australia.

[7] Department of Biochemistry and Chemistry, La Trobe University, Melbourne, Australia.

[8] School of Science, STEM College, RMIT University, Melbourne, Australia

[9] St Vincent's Institute of Medical Research, Fitzroy, Australia

[10] Department of Medicine, Eastern Hill Academic Centre, Melbourne Medical School, The University of Melbourne, Carlton, Australia

[11] La Trobe University Bioimaging Platform, Bundoora, Victoria, Australia

[12] Charles Perkins Centre and School of Life and Environmental Sciences, The University of Sydney.

*Correspondence: k.helbig@latrobe.edu.au and e.monson@latrobe.edu.au

† These authors contributed equally to this work.

**Key words:** lipid droplets, virus, RNA, lipidomics, proteomics, dual omics, signalling, antiviral, innate immunity

**Abstract:** Lipid droplets (LDs), once viewed as inert lipid storage sites, are now recognised as dynamic organelles central to cellular signalling and immunity. This study presents a dual-omics approach, integrating proteomics and lipidomics, to investigate LDs in the host antiviral response. *In vivo* and *in vitro* RNA viral infection models demonstrate that LDs rapidly remodel both their proteome and lipidome. The antiviral proteins RIG-I, MDA5, STAT1, STAT2, and viperin are specifically recruited to virus-induced LDs. Simultaneously, the LD lipidome shifts toward enrichment in long-chain polyunsaturated fatty acids and bioactive phospholipids, likely enhancing membrane dynamics and protein recruitment. Enzymes involved in lipid metabolism and post-translational modifications are also upregulated, suggesting a mechanistic link between lipid remodeling and protein localisation. Functional assays utilizing artificial LDs revealed that arachidonic-acid and eicosapentaenoic-acid suppress viral replication and enhance type I and III interferon responses. These findings position LDs as key immunometabolic platforms in early antiviral defence.

# Introduction

Lipid droplets (LDs) are present in the different cell types of all living organisms. Once thought to function solely as passive energy reservoirs, LDs are now recognised as highly dynamic cytoplasmic organelles that play critical roles in a wide range of signalling pathways (*1–3*). Unlike other organelles that are surrounded by a phospholipid bilayer, LDs are enclosed by a single phospholipid monolayer that encapsulates a neutral lipid core. Their surfaces are also decorated with proteins that are believed to drive their cellular functions (*4*, *5*), with recent advances in proteomic technologies revealing the high diversity of the LD proteome.

In mammals, LDs are upregulated by the host in multiple disease states, including cancer, cardiovascular disease, neurodegenerative disorders, and following infection of cells with bacteria, fungi, parasites and viruses (reviewed in (*6–9*)). Historically, LDs were thought to serve primarily as nutrient-rich reservoirs exploited by pathogens for energy and lipid synthesis, however, emerging evidence reveals a more complex role for LDs in immunity with host-derived LDs actively contributing to cell survival following pathogen infection. They have been shown to recruit and concentrate antimicrobial proteins, and can act as platforms for innate immune signalling, including the induction of pro-inflammatory cytokines and interferon responses (*10–12*), highlighting LDs as not only metabolic hubs but also key players in the host defence machinery.

A successful innate immune response to virus infection requires LD upregulation (*10*). In particular, during zika virus (ZIKV) and herpes simplex virus -1 (HSV-1) infection, LD's upregulated via non-homeostatic mechanism involving engagement of the EGFR, has been linked to the downstream production of type-I and III interferons (IFNs; IFN-β and IFN- λ) (*10*). However, the mechanism underpinning this increase in IFN production remains elusive and may involve both changes in lipid and protein profiles. Successful antiviral responses rely on complex protein-protein interactions that require platforms for their assembly (*1*, *13–15*). LDs house viperin, a key antiviral protein that also regulates multiple antiviral signalling cascades (*1*, *2*, *14*), but beyond this, the role of LDs in facilitating other protein complex formations remains unknown. The LD proteome is both diverse and dynamic in nature, changing constantly to cellular cues, and we now know that changes in lipid species can drive alternate protein binding across cellular membranes (*16–19*). Specific lipids have also been shown to influence antiviral cytokine

expression, in particular cellular cholesterol reduction can trigger antiviral signalling and there is a complex relationship between bioactive lipids and antiviral control (*20*).

Given the recent recognition of LDs as essential organelles in host driven antiviral immunity, and the emerging appreciation of the intricate interplay between proteins and lipids, here we describe the development of technologies that, for the first time, enable simultaneous analysis of the LD proteome and lipidome in mammalian cells. Using these approaches, we demonstrate that LDs undergo rapid and coordinated changes in both protein and lipid composition in response to viral infection. These changes include the recruitment of key antiviral proteins and modifications in long-chain fatty acid content, which together support an effective antiviral response and contribute to broader host cell signalling processes.

# Results

***Brain derived lipid droplets recruit cellular defence proteins following LCMV infection in vivo.*** LDs are upregulated early following viral infection in mammalian cells and are essential for the production of a heightened antiviral IFN state (*10*), however, the mechanisms that underpin their ability to drive IFN production and limit early viral replication remain unknown. To investigate the role upregulated LDs may play in cellular restriction of viral infection we selected a well-established neural model of lymphocytic choriomeningitis virus (LCMV) infection (*21*). Mice were infected with LCMV intracranially, and their brains were harvested at 2- and 4-days post infection (dpi), modelling early-stage infection, as evidenced by increases in viral load and cytokine expression (Fig 1A, 1B, S1A, S1B). LD abundance was significantly increased in the brains of virally infected mice at both 2 and 4 dpi (Fig 1B, 1C and S1C), as we have also previously observed *in vivo* during influenza A and dengue viral infection in the lungs and brain respectively (*10*). To further characterize the potential role of LDs in viral infection we developed techniques to cleanly extract LDs from whole murine brains (S1C, 1D) and performed comparative mass spectrometry profiling of proteins differentially associated with LCMV-LDs or SHAM-LDs isolated from the brain tissues of mice. In the virally infected brains, 4324 proteins were identified on LDs (Fig 1D; Table S1; S1E). Of these, only 30 were found to be differentially upregulated compared to SHAM-LDs, with 24 proteins exclusively upregulated on LCMV-LDs, and only 2 downregulated (0.5%; Fig 1D-F and S1E). Functional annotation enrichment analysis revealed that most of the upregulated LD proteins at 4 dpi belonged to ‘cellular defence response to viruses’

and ‘response to interferons’ (Fig 1G), the predominant mammalian antiviral cytokines. Additionally, the enrichment of proteins within our LD subsets following viral infection did not follow the identical enrichment patterns within the whole cell lysate, further illustrating that LDs enrich specific proteins following viral infection (Fig 1H).

The brain contains a very heterogenous mix of cell types, and LCMV has been demonstrated previously to infect both neurons and astrocytes (*22*). To assess the cell type specificity of the upregulation of LDs in our LCMV model of murine brain infection we next performed immunofluorescence analysis on fresh frozen brain sections (Fig S2). Both microglia and neurons were shown to express LD, although at lower levels, with no significant increase seen following viral infection. However, astrocytes demonstrated more than a two-fold increase in LDs following LCMV infection, showing them to be the largest contributor in the brain to the upregulated LD response to virus (Fig 1I, S2).

# Figure 1.

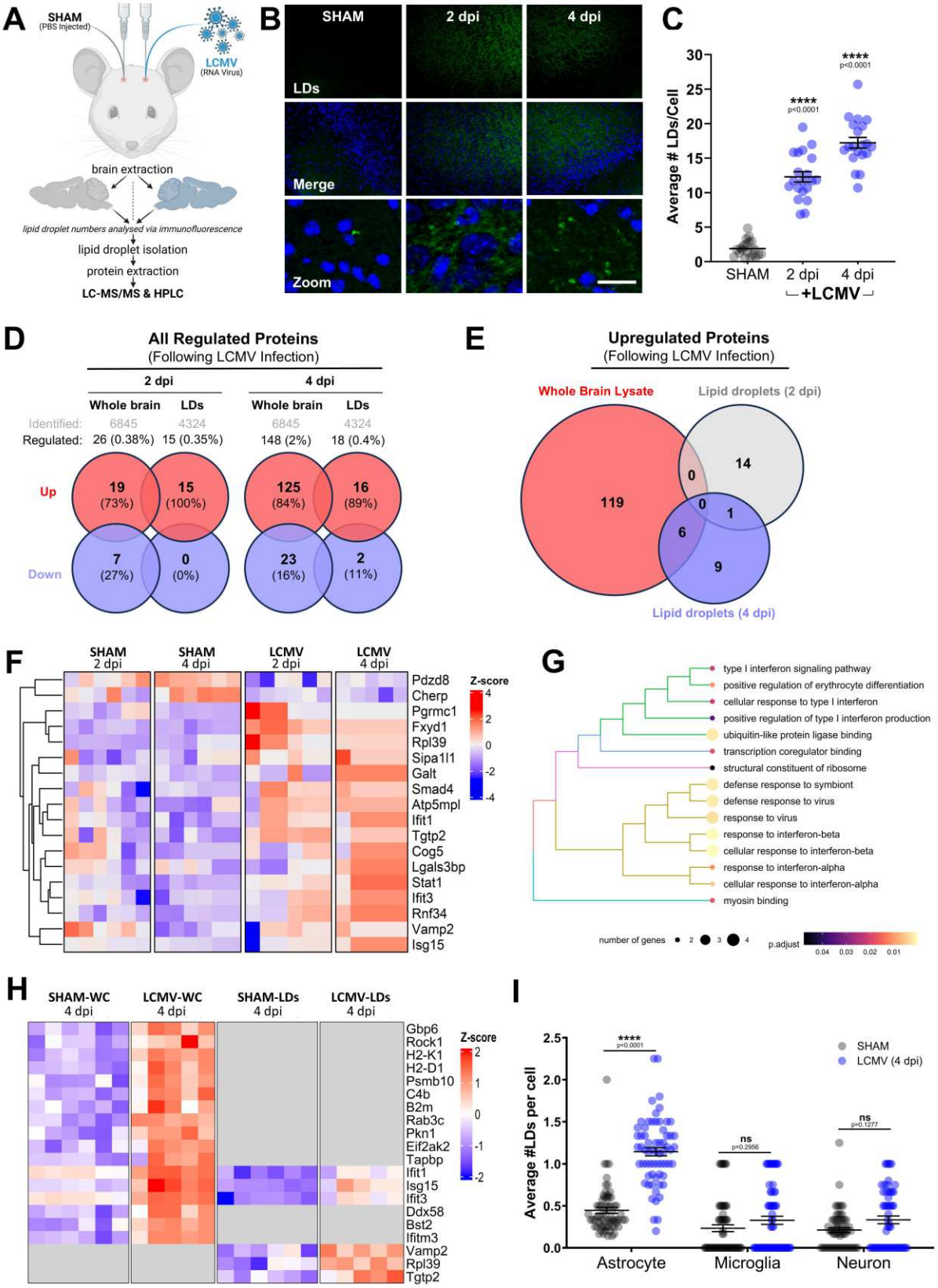
A
SHAM
(PBS Injected)
LCMV
(RNA Virus)
brain extraction
lipid droplet numbers analysed via immunofluorescence
lipid droplet isolation
protein extraction
LC-MS/MS & HPLC
B
SHAM
2 dpi
4 dpi
LDs
Merge
Zoom
C
Average # LDs/Cell
****
p<0.0001
SHAM
2 dpi
4 dpi
+LCMV
D
All Regulated Proteins
(Following LCMV Infection)
2 dpi
4 dpi
Whole brain
LDs
Identified:
6845
4324
6845
4324
Regulated:
26 (0.38%)
15 (0.35%)
148 (2%)
18 (0.4%)
Up
Down
19 (73%)
15 (100%)
125 (84%)
16 (89%)
7 (27%)
0 (0%)
23 (16%)
2 (11%)
E
Upregulated Proteins
(Following LCMV Infection)
Whole Brain Lysate
Lipid droplets (2 dpi)
Lipid droplets (4 dpi)
119
0
14
0
1
6
9
F
SHAM 2 dpi
SHAM 4 dpi
LCMV 2 dpi
LCMV 4 dpi
Z-score
Pdzd8
Cherp
Pgrmc1
Fxyd1
Rpl39
Sipa1l1
Galt
Smad4
Atp5mpl
Ifit1
Tgtp2
Cog5
Lgals3bp
Stat1
Ifit3
Rnf34
Vamp2
Isg15
G
type I interferon signaling pathway
positive regulation of erythrocyte differentiation
cellular response to type I interferon
positive regulation of type I interferon production
ubiquitin-like protein ligase binding
transcription coregulator binding
structural constituent of ribosome
defense response to symbiont
defense response to virus
response to virus
response to interferon-beta
cellular response to interferon-beta
response to interferon-alpha
cellular response to interferon-alpha
myosin binding
number of genes
p.adjust
H
SHAM-WC 4 dpi
LCMV-WC 4 dpi
SHAM-LDs 4 dpi
LCMV-LDs 4 dpi
Z-score
Gbp6
Rock1
H2-K1
H2-D1
Psmb10
C4b
B2m
Rab3c
Pkn1
Eif2ak2
Tapbp
Ifit1
Isg15
Ifit3
Ddx58
Bst2
Ifitm3
Vamp2
Rpl39
Tgtp2
I
Average #LDs per cell
****
p<0.0001
ns
p=0.2956
ns
p=0.1277
SHAM
LCMV (4 dpi)
Astrocyte
Microglia
Neuron

122

**Figure. 1. LCMV infection upregulates lipid droplets and drives lipid droplet proteomic changes *in vivo*. (A)** Study overview: Mice were intracranially SHAM or LCMV (500 PFU) infected n= 6 replicates were taken from mice samples (SHAM 2 dpi, LCMV 2 dpi, SHAM 4 dpi, LCMV 4dpi). **(B)** Mice brains were harvested, and half of the brains were sectioned for immunostaining. LDs were stained with Bodipy (493/503) (green) and nuclei with DAPI (blue). Scale bar, 100μm. **(C)** LD numbers were analysed via ImageJ analysis software. Error bars represent ± SEM, n = 6 replicate mice per condition. **(D)** Comparative analysis of protein ID and abundance were analysed by LC-MS/MS highlighting the number of proteins significantly regulated from both whole brain lysate and isolated LD lysate derived from mice brains following 2 and 4 dpi of LCMV. Red and blue circles indicate up- and down regulated proteins, respectively. **(E)** Significantly upregulated proteins following LCMV infection (compared to SHAM) were compared with one another to highlight distinct proteomic profiles between LDs and whole brain lysates. The red circle reflects proteins exclusive to the whole brain lysate; the grey circle reflects proteins exclusive to LDs 2 dpi and the blue circle reflects proteins exclusive to LDs 4 dpi. **(F)** Hierarchical clustering of the 18 significantly regulated LD resident proteins 4 dpi of LCMV across replicates and their respective z-scores from the groups: control 2 dpi, control 4 dpi, LCMV 2 dpi and LCMV 4 dpi. Blue tiles refer to proteins with a z-score < 0 with red tiles referring to proteins with a z-score > 0. **(G)** Tree-plot displaying similarity clusters of the top 15 significantly enriched annotations from the gene ontology categories: Biological Process (BP), Molecular Function (MF) and Cellular Component (CC). Only annotations that surpassed an adjusted p-value of less than 0.05 were included. **(H)** Hierarchical clustering comparing the significantly upregulated proteins (annotated to be involved in "immune response to virus" using the UniProt database) 4 dpi with SHAM or LCMV in both whole brain lysate and LD lysate highlighting different proteomic signatures following viral infection. Blue tiles refer to proteins with a z-score < 0 with red tiles referring to proteins with a z-score > 0. (**I**) Analysis of average number of LDs localised to each brain cell type with and without LCMV 4 dpi. Error bars represent values ± SEM. *P* values were determined by two-way ANOVA post-hoc pairwise comparisons with Bonferroni correction (n= 64 tissue sections over 6 mice).

***Astrocyte lipid droplets recruit immune signalling proteins following viral infection.***

We next wanted to gain an astrocyte cell-type specific LD proteomic profile following response to viral infection. To do this in the absence of viral antagonism, we first described the proteomic shift of LDs following RNA viral mimic stimulation of early innate antiviral signalling pathways using dsRNA in primary immortalised astrocyte cells *in vitro*. As described previously by our team (*10*), an upregulation of LDs was observed at both 8 and 24 hrs following dsRNA stimulation (Fig S3A). The proteomic profiles of isolated LDs revealed an upregulation of 10 and 56 proteins at 8 and 24 hrs respectively following stimulation of cells with dsRNA (Fig 2A, B, S3B and table S2). Functional categorisation of the entire LD proteome (Fig 2Ci) in comparison to the differentially regulated LD proteins following stimulation (24 hrs, Fig 2Cii) revealed an altered distribution of LD proteins that saw an increase of proteins belonging to the 'immune response' and 'lipid metabolism' functional categories (Table 2).

Astrocytes have a robust immune response following viral infection (*23*, *24*). Of the 'immune response' category proteins shown to be upregulated in the whole cell following viral mimic stimulation, only a sub-set of these proteins were recruited to the LD (Fig 2D), including IFIT3, DDX58 (RIG-I), ISG15, IFIT2, IFIT1, MX1, STAT1, RSAD2 (viperin). Using STRING (Search Tool for the Retrieval of Interacting Genes/Proteins) network analysis, these immune response proteins were seen to have a high level of predicted protein-protein interactions with each other, which also included interactions with CMPK2, a known interaction partner of RSAD2 required for its antiviral function (Fig 2E) (*25*). Other clusters observed with our upregulated LD proteins included interactions networks of Rab proteins and lipid metabolism proteins (LPCAT1, ACSL3, ACSL4, LSS, SQLE, HSD17B7, SDHL, LPCAT2, FAF2).

Members of the 'immune response' category of proteins were also upregulated on the LD following an RNA viral infection (zika virus) of the astrocyte cells at the same time point (24 hrs: Fig 2F, Fig S3C and Table S3). Immunoblotting of LD fractions confirmed the presence of selected novel LD localised proteins, at steady state or upregulated following dsRNA stimulation (Fig 2G). These results indicate that key antiviral proteins localise to the LD following activation of viral RNA sensors by either a viral mimic or active RNA viral infection.

# Figure 2.

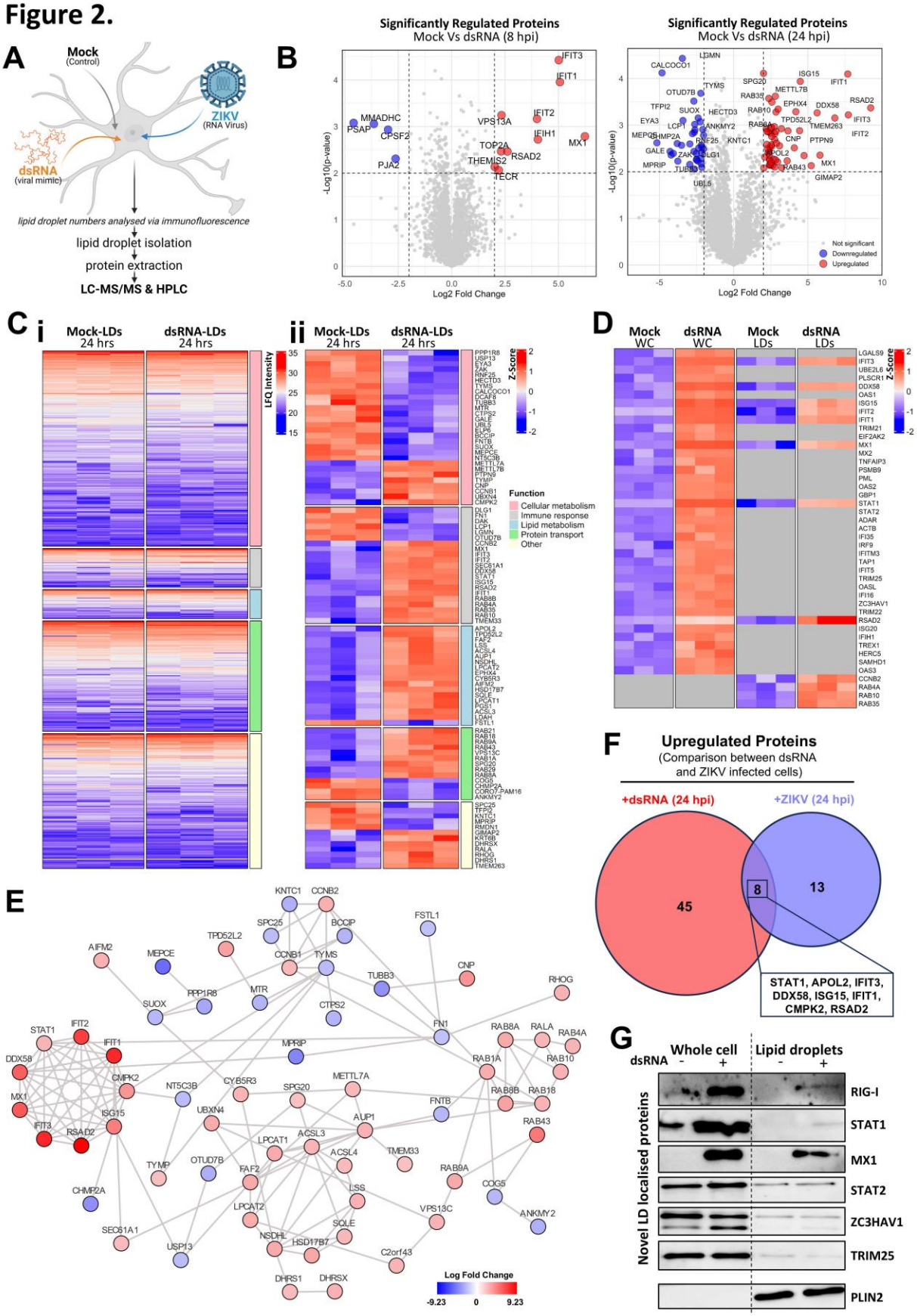
A
Mock
(Control)
ZIKV
(RNA Virus)
dsRNA
(viral mimic)
lipid droplet numbers analysed via immunofluorescence
lipid droplet isolation
protein extraction
LC-MS/MS & HPLC
B
Significantly Regulated Proteins
Mock Vs dsRNA (8 hpi)
Significantly Regulated Proteins
Mock Vs dsRNA (24 hpi)
-Log10(p-value)
Log2 Fold Change
Not significant
Downregulated
Upregulated
C
i
ii
Mock-LDs
24 hrs
dsRNA-LDs
24 hrs
LFQ Intensity
Z-Score
Function
Cellular metabolism
Immune response
Lipid metabolism
Protein transport
Other
D
Mock
WC
dsRNA
WC
Mock
LDs
dsRNA
LDs
Z-Score
E
Log Fold Change
F
Upregulated Proteins
(Comparison between dsRNA
and ZIKV infected cells)
+dsRNA (24 hpi)
+ZIKV (24 hpi)
45
8
13
STAT1, APOL2, IFIT3,
DDX58, ISG15, IFIT1,
CMPK2, RSAD2
G
Whole cell
Lipid droplets
dsRNA
Novel LD localised proteins
RIG-I
STAT1
MX1
STAT2
ZC3HAV1
TRIM25
PLIN2

183

**Figure 2: Proteomic profiling of astrocyte RNA-LDs reveals recruitment of novel immune signalling proteins. (A)** Study overview: human primary immortalised astrocyte cells were either mock infected or infected with the dsRNA viral mimic: Poly(I:C) or infected with the ZIKV (MOI 1). LDs were isolated from cells post infection. n= 3 biological replicates were used for proteomic analysis. **(B)** Differentially expressed genes dsRNA-LDs compared to mock 8 and 24 hpi were analysed via a volcano plot (n= 3 replicates per condition). **(C) (i)** Hierarchical clustering of the 3870 identified LD proteins from astrocyte cells and their respective abundance in mock or dsRNA stimulation (24 hpi) conditions. Proteins were grouped according to gene ontology annotations (n= 3 replicates per condition). Gene ontology was performed using the Uniprot database within Perseus. Proteins were grouped into 5 main categories: *cellular metabolism*, *immune response*, *lipid metabolism*, *protein transport* and *other*. **(ii)** Hierarchical clustering displaying the z-scores and gene ontology between replicates of the 92 significantly regulated astrocyte derived LD proteins following dsRNA stimulation at 24 hrs. Blue tiles refer to proteins with a z-score < 0 with red tiles referring to proteins with a z-score > 0. Gene ontology was performed using the Uniprot database within Perseus. Proteins were grouped into 5 main categories: *cellular metabolism, immune response, lipid metabolism, protein transport and other*. **(D)** Heatmap displaying the z-scores of the significantly regulated immune proteins identified in either whole cell or LD lysates 24 hrs following dsRNA stimulation. Blue tiles refer to proteins with a z-score < 0 with red tiles referring to proteins with a z-score > 0 and grey tiles represent no expression due to a lack of significance in the respective conditions**. (E)** Interaction diagram of significantly changed proteins following dsRNA stimulation created using STRING confidence scores and interactions in cytoscape. Nodes were coloured in a continuous scale based off their log2 fold change, with red coloured nodes having the highest fold change and blue nodes representing the greatest negative fold change. Proteins with no interactions with any other proteins were not represented within the network. All clusters were clustered using the ClusterONE plugin within cytoscape with a $p < 0.05$ significance threshold. **(F)** Comparative analysis was performed between significantly enriched proteins from astrocyte derived LDs infected with either dsRNA or ZIKV (MOI 1) at 24 hrs respectively. Red circle highlights proteins exclusive to dsRNA stimulation with the blue circle representing proteins exclusively enriched following ZIKV infection and the crossover of these two highlighting the proteins regulated between both conditions. **(G)** Immunoblot analysis on whole cell lysate and isolated LD lysate from both mock and dsRNA stimulated astrocytes at 24 hrs confirmed the localisation of MX1, RIG-I, STAT1, STAT2, ZC3HAV1 and TRIM25 proteins on isolated LDs derived from cells that have been stimulated with dsRNA for 24 hrs. PLIN2 was used to confirm enrichment of purified LDs, image represents n=3.

***STAT proteins dynamically localise to lipid droplets following virus infection in vitro.***

To date the only antiviral protein shown to localise to LDs in human cells is viperin (RSAD2), which orchestrates a heightened antiviral environment (2, 19, 20). Our proteomic analysis of LDs in primary immortalised astrocyte cells revealed that multiple members of the early antiviral innate immune signalling pathways thought previously to be cytoplasmic were present in the LD proteome, with expression of selected proteins being significantly upregulated following both pathway activation by dsRNA (in the absence of viral-mediated antagonism) or ZIKV infection (Fig 2A,B, F; Table S2,3). Many of these proteins are known to be involved in early antiviral signalling pathways or have known antiviral functions (Fig 3A), including STAT1 and STAT2, which underpin the formation of the ISGF3 complex that initiates transcription of multiple antiviral proteins (*26*). To further confirm the ability of the STATs to localise to LDs we performed microscopy analysis. Confocal imaging confirmed the known LD localised protein, viperin (21, 22), to be highly abundant on the outside of LDs, with novel localised proteins; STAT1 and STAT2 being less abundant on LDs, and colocalising to only a subset of cytoplasmic LDs following activation of innate immune pathways by dsRNA (Fig 3B). To more confidently validate the localisation of these proteins to the LD and enumerate the percentage of LDs these antiviral proteins were localising to, we isolated LDs from cells overexpressing tagged mCherry-viperin, -STAT1, and -STAT2 (Fig S4A). Viperin was present on 54.8% of LDs on average, in comparison to STAT1 localising to 44.9% and STAT2, 24.9%, which was also confirmed via immunoblotting (Fig 3C-E).

Further confirmation of native STAT1 localisation to the LD, and its phosphorylated forms (STAT1-Tyrosine701; ph-STAT1(T) and STAT1-Serine 727; ph-STAT1(S)), was performed using super resolution microscopy (single molecule localisation microscopy, SMLM), where we tracked STAT1 co-localisation with LDs in the cell over a timeframe of 72 hrs post dsRNA stimulation (Fig 3F, G and S4B). There was a significant increase in the number of co-localisation events of LDs with both STAT1 and ph-STAT1(T) at multiple time points (Fig 3F, G), with no significant increase in association observed between ph-STAT1(S) and LDs. However, the interaction of ph-STAT1 (T) with the LD was the most significantly enhanced interaction from as early as 8 hrs post activation of early innate antiviral signalling pathways, when normalised to the increased cellular density of both LDs and STAT1 proteins (Fig 3G; S4B, S4C). This was further supported by a doubling of non-random co-localisation events between the LD and ph-STAT1(T)

252 by 48 hrs post activation in which the degree of colocalisation was equivalent to random levels of
253 overlap as indicated by values over 1 (Fig S4B).

254

255 We have previously shown that virally driven LDs are upregulated via a non-homeostatic
256 mechanism dependant on EGFR activation (*10*). To assess whether the localisation of either total
257 STAT1 or ph-STAT(T) was altered during inhibition of virally driven LDs we performed the
258 above experiments again in the presence of an EGFR inhibitor (Fig 4). When normalising back to
259 cellular LD number and STAT protein expression, we saw that loss of EGFR signalling
260 significantly decreased the ability of both STAT1 and phSTAT-1(T) to localise to LDs. Indicating
261 that these proteins preferentially bind to virally driven LDs.

262

263

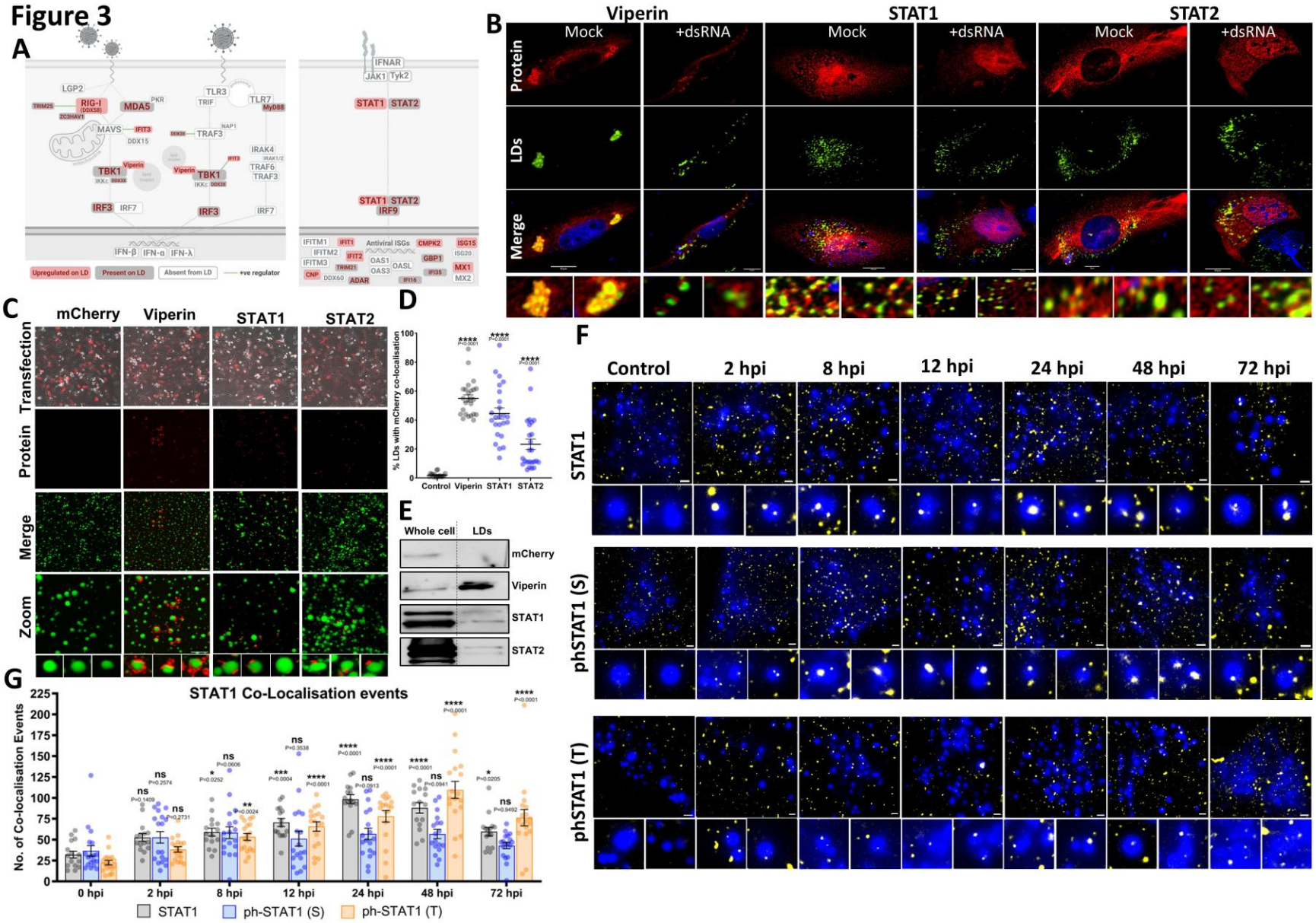
Figure 3
A
LGP2
RIG-I
MDA5
PKR
TLR3
TRIF
TLR7
MyD88
MAVS
IFIT3
DDX15
TRAF3
IRAK4
TRAF6
TBK1
Viperin
IRF3
IRF7
IFN-β
IFN-α
IFN-λ
Upregulated on LD
Present on LD
Absent from LD
+ve regulator
IFNAR
JAK1
Tyk2
STAT1
STAT2
IRF9
Antiviral ISGs
B
Viperin
STAT1
STAT2
Mock
+dsRNA
Protein
LDs
Merge
C
mCherry
Viperin
STAT1
STAT2
Transfection
Protein
Merge
Zoom
D
% LDs with mCherry co-localisation
Control
Viperin
STAT1
STAT2
E
Whole cell
LDs
mCherry
Viperin
STAT1
STAT2
F
Control
2 hpi
8 hpi
12 hpi
24 hpi
48 hpi
72 hpi
STAT1
phSTAT1 (S)
phSTAT1 (T)
G
STAT1 Co-Localisation events
No. of Co-localisation Events
0 hpi
2 hpi
8 hpi
12 hpi
24 hpi
48 hpi
72 hpi
STAT1
ph-STAT1 (S)
ph-STAT1 (T)

**Fig 3. STAT proteins localise to lipid droplets. (A)** Schematic of the interferon signalling pathway following viral infection with proteins absent from the LD proteome in white, proteins present on the LD proteome in grey and proteins upregulated on the LD in red, based on data from RNA stimulation at 24 hrs. **(B)** Primary immortalised astrocyte cells were transfected with a mCherry tagged viperin, STAT1 and STAT2 (red) and cells were stained with Bodipy (493/503) to visualise LDs (green) and DAPI to visualise cell nuclei (blue). The zoomed images indicate interaction between the respective mCherry tagged proteins and LDs. Scale bar, 50μm. **(C)** Confocal microscopy of astrocytes transfected with mCherry, viperin-mCherry, STAT1-mCherry and STAT2-mCherry respectively, with LDs then isolated and purified. Purified LDs were then imaged to determine the interaction between viperin, STAT1 and STAT2 with LDs. The zoom panel highlights the localisation of the proteins with isolated and purified LDs. Scale bar, 400 μm for transfection panels, 50 μm for merge and 20 μm for zoom panels. **(D)** Isolated LDs were also imaged to allow the quantification of the percentage of LDs that have mCherry co-localisation with each data point representing the average percentage of co-localisation in a field of view of ~500-3000 LDs (n=18-25) over 2 independent experiments. Error bars represent ± SEM. **(E)** To further validate the confocal microscopy of isolated LDs, the purified LDs and the whole cell lysates from the transfected astrocytes were immunoblotted for mCherry to show detection of mCherry tagged proteins, image represents n=3. **(F)** LD-STAT1 co-localisation events were visualised post dsRNA transfection via super resolution microscopy: Single-molecule localisation microscopy (SMLM). The epifluorescence images of LDs were merged with the SMLM images of STAT1 (STAT1, ph-STAT1 (S; serine 727)/ (T; tyrosine 701)), and co-localisation events counted across a 72 hrs dsRNA stimulation time course. Cells were immunolabelled and imaged for LDs (Bodipy (493/503), epi, blue) and STAT1 (AlexaFluor647, SMLM, yellow). (n = 3 independent biological replicates). Scale bars represent 5 μm, with zoom inserts representing 2 μm x 2 μm in size. **(G)** LD-STAT1 co-localisation data was quantified as number of co-localisation events per cell. Raw super-resolution data was analysed and rendered using the ThunderSTORM plugin in ImageJ before merging with epifluorescence LD images and enumeration of co-localisation events. Error bars represent ± SEM, n= 30 cells over 3 independent assays.

## Figure 4.

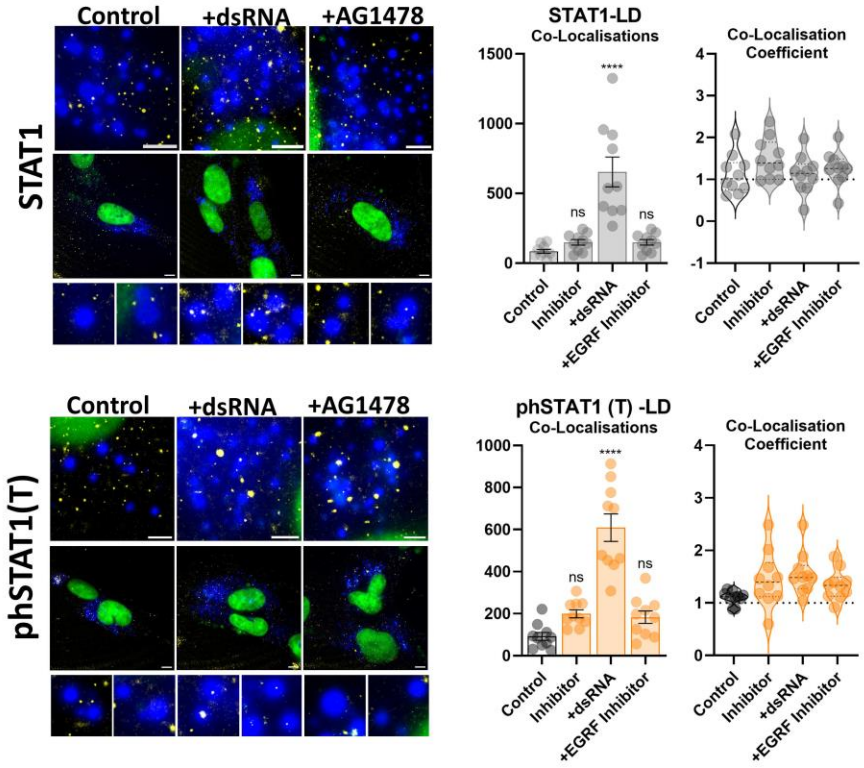


294
295 **Figure 4. STAT protein localisation to lipid droplets is EGFR driven.** Primary immortalised
296 astrocyte cells were treated with 2 µM AG-1478 (EGFR inhibitor) 16 h prior to stimulation with
297 dsRNA for 24 h. LD-STAT1 co-localisation events were visualised with single-molecule
298 localisation microscopy (SMLM). The epifluorescence images of LDs were merged with the
299 SMLM images of STAT1 and ph-STAT1 (T; tyrosine 701). Cells were immunolabelled and
300 imaged for LDs (Bodipy (493/503), epi, blue) and STAT1 (AlexaFluor647, SMLM, yellow). (n =
301 3 independent biological replicates). Scale bars represent 5 µm, with zoom inserts representing 2
302 µm x 2 µm in size. Raw super-resolution data was analysed and rendered using the
303 ThunderSTORM plugin in ImageJ before merging with epifluorescence LD images and
304 enumeration of co-localisation events. Error bars represent ± SEM, n= 10 cells over 3 independent
305 assays.

306

307

***Lipid droplets interact with mitochondria to form signalosome complexes***

Our proteomic analysis of virally driven LDs also demonstrated that both major viral RNA sensors form part of the LD proteome: MDA5 at baseline, as well as upregulated RIG-I (DDX58) following both ZIKV infection and dsRNA stimulation (Fig 3A, Fig 2, Supp Table 2 and 3). Both of these RNA sensors require subsequent interaction with Mitochondrial Antiviral Signaling (MAVS) to drive antiviral cytokine expression, which is predominantly expressed on the mitochondria and is absent from the LD proteome ((*27*), Fig 5A). We hypothesied that LDs may assist in signalosome formation of RIG-1 to facilitate activation of the RNA sensor adaptor protein, MAVS.

We first examined if LDs enhanced their interaction with mitochondria following viral infections. Live cell imaging analysis of astrocytes revealed that the frequency of LDs interacting with mitochondria increased significantly during both dsRNA and ZIKV infection, a phenomenon that did not occur when increasing LD numbers via oleic acid treatment of the cells (Fig 5B-G, S5, Supp Movie 1-4). This increase in interactions was driven by transient interactions of LD and mitochondria (Fig 5D, E), with some LDs interacting with mitochondria up to 15 times in a 10-minute timeframe, with an average of 6 interactions in virally infected cells compared to 1.8 in mock cells (Fig 5F, G). Using confocal microscopy to image RIG-I and MAVS on the surface of both LDs and mitochondria we observed multiple instances of signalosome formation in individual cells, with LD localised RIG-I forming complexes with mitochondrial localised MAVS, following activation of early innate signalling pathways with an RNA viral mimic (Fig 5H, Fig S6A).

The structure of RIG-I displays no obvious structural features that would allow it to bind to a phospholipid membrane (Fig 6A). To understand how RIG-1 is localising to the LD surface, we screened the protein structure using the DisoLipPred web server (*28*) for disordered lipid binding regions (DLBRs). We found that RIG-1 contains four main identifiable regions of DLBRs with 24 of the 925 (3%) amino acid residues consisting of amino acids that have a propensity to form DLBRs (Fig 6B). We next used computational modelling to determine if a complex between RIG-I and the phospholipid monolayer of a LD was possible. The cryo-EM structure of a viral RNA mimetic in complex with RIG-1 (PDB code: 7TNY, (*29*)) was docked onto a POPC lipid bilayer (to mimic a LD) and subjected to molecular dynamics simulations to determine if this interaction was stable. Across the 10nS simulation, there was little change in energy or RMSD, indicating a stable interaction between a lipid and the protein (Fig 6 and S6B). This model suggests that LDs

are able to interact with the Hel2 of RIG-I, shown to be essential as an autoinhibitory motif of RIG-I. This model would also leave the CARD domains of RIG-I free to interact with MAVS via the well-established mechanism (*30*). In summary, the modelling supported the formation of a signalosome between LDs, RIG-I, MAVs and the mitochondria (*29*).

## Figure 5.

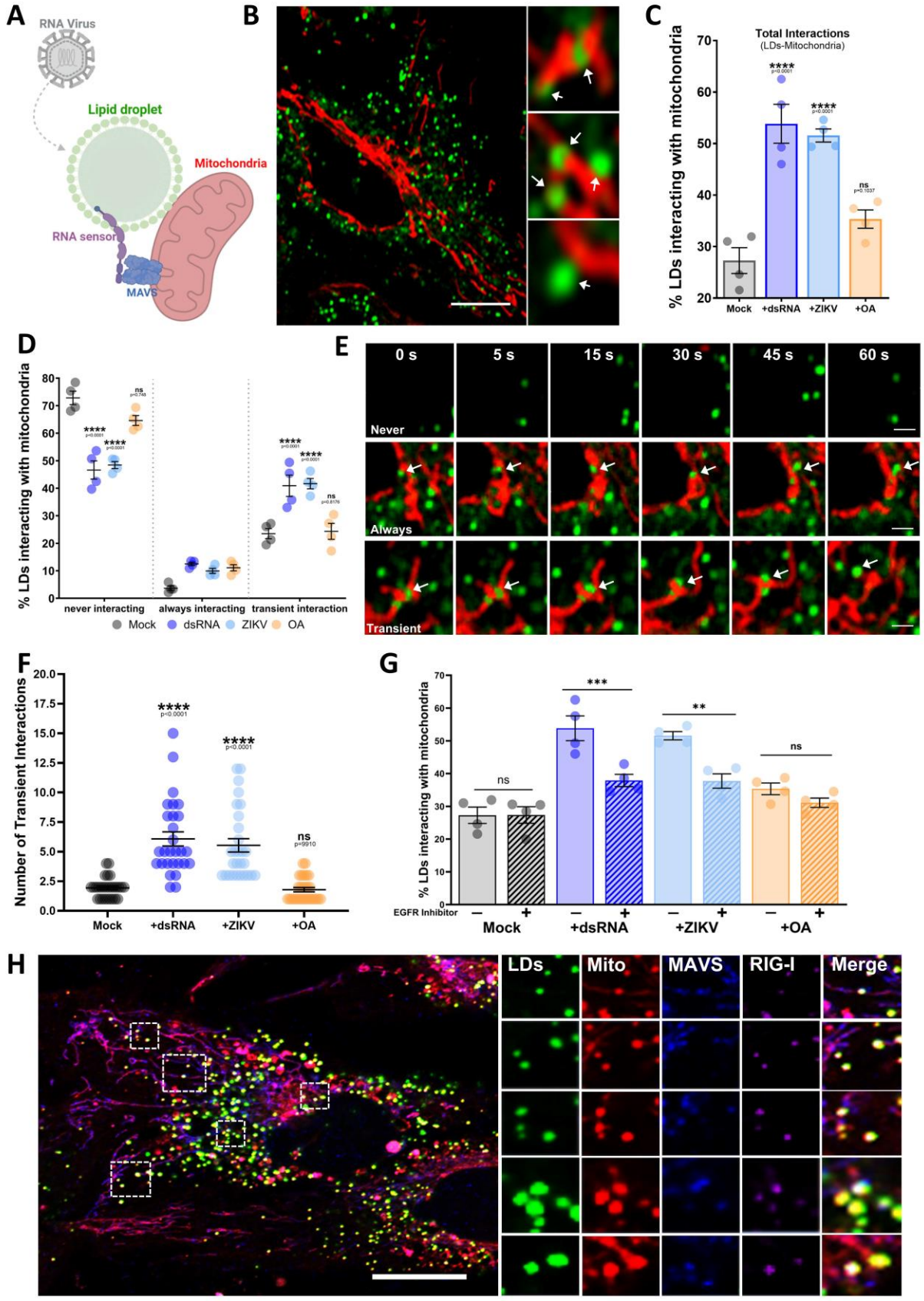
A
RNA Virus
Lipid droplet
Mitochondria
RNA sensor
MAVS
B
C
Total Interactions
(LDs-Mitochondria)
% LDs interacting with mitochondria
Mock
+dsRNA
+ZIKV
+OA
D
% LDs interacting with mitochondria
never interacting
always interacting
transient interaction
Mock
dsRNA
ZIKV
OA
E
0 s
5 s
15 s
30 s
45 s
60 s
Never
Always
Transient
F
Number of Transient Interactions
Mock
+dsRNA
+ZIKV
+OA
G
% LDs interacting with mitochondria
EGFR Inhibitor
Mock
+dsRNA
+ZIKV
+OA
H
LDs
Mito
MAVS
RIG-I
Merge

343

**Fig 5: Lipid droplets interact with mitochondria to form a signalosome with RIG-1 and MAVS. (A)** Schematic depiction of the potential signalosome interaction between RIG-I localised to the LD surface and MAVS, localised to the mitochondria surface. **(B)** Primary immortalised astrocyte cells were transfected with a RIG-I over expression plasmid and stimulated with dsRNA for 24 hrs. Cells were live stained with MitoTracker Red prior to fixation and then all cells were stained with Autodot LD dye to visualise LDs (green), αRIG-I antibody (1:200) (purple) and αMAVS antibody (1:100) (blue). Scale bar, 50 μm. **(C)** Primary immortalised astrocyte cells were live stained with Bodipy (493/503) to visualise LDs (green) and MitoTracker Red to visualise mitochondria (red) and were live imaged on a Zeiss800 confocal over a 10 min timeframe. White arrows indicate interactions between the two organelles. Scale bar, 50 μm. **(D-G)** Cells were live stained, and infected with either ZIKV (MR766 strain) at an MOI1, stimulated with dsRNA viral mimic (Poly I:C) or treated with oleic acid (OA, 500 μM) for 8 hrs, and imaged for LD/mitochondria movement in live stimulated cells for 10 mins (120 frames). Images were analysed via Imaris image software for % interactions between LDs and mitochondria, and data was further analysed for numbers of transient interactions between the two organelles. n= 100 cells across 6 fields of view over 3 biological replicates, scale bar, 50 μm. **(H)** Primary immortalised astrocyte cells were transfected with a RIG-I over expression plasmid and stimulated with dsRNA for 24 hpi. Cells were live stained with MitoTracker Red prior to fixation and all cells were stained with Autodot LD dye to visualise LDs (green), αRIG-I antibody (1:200) (purple) and αMAVS antibody (1:100) (blue). Scale bar, 50 μm.

Figure 6.

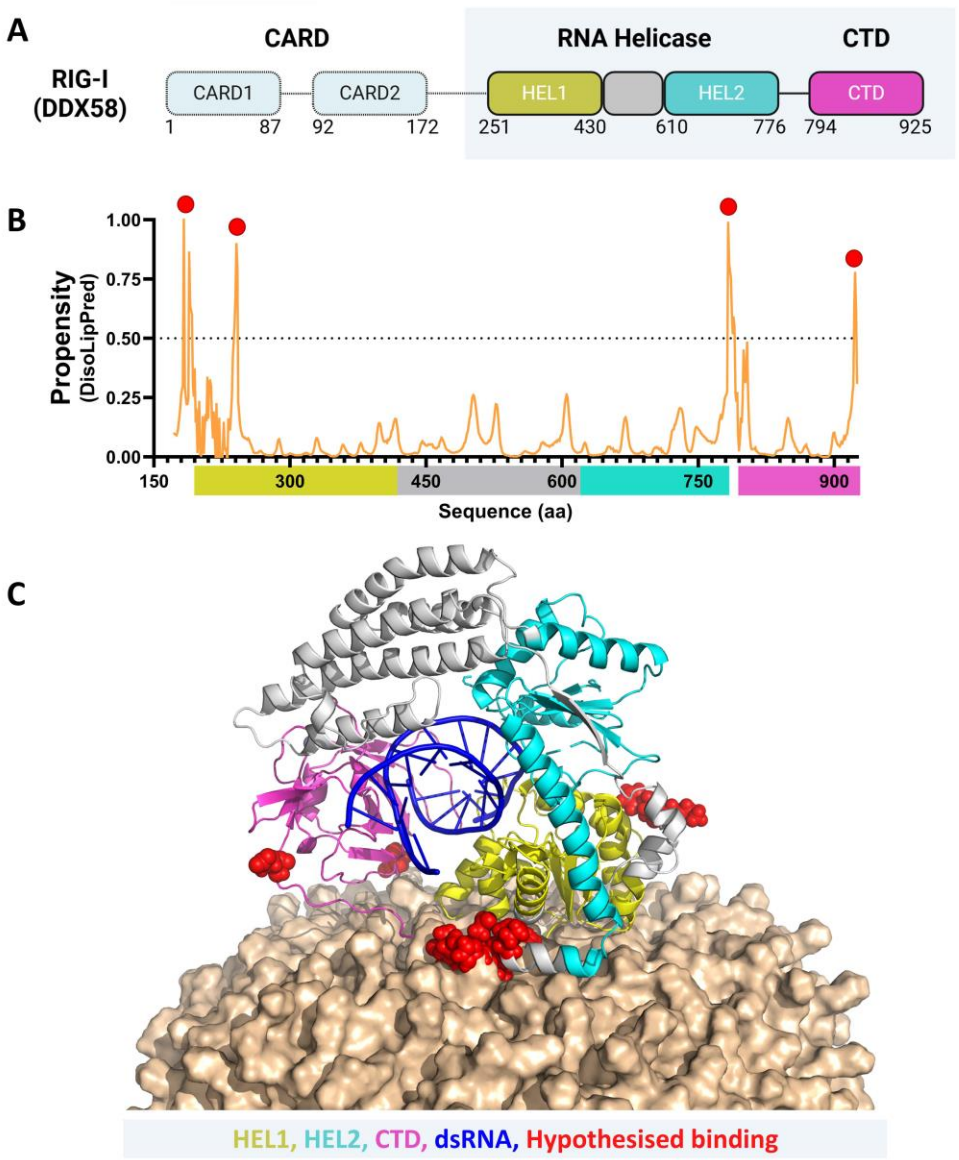


**Fig 6: Structural Modelling reveals that RIG-1 localises to lipid droplet membrane**

**(A)** Domain architecture of RIG-1. RIG-1 contains contain two caspase activation and recruitment domains (CARDs) in tandem orientation at their N termini, an RNA helicase domain and a RNA-binding fold, called the carboxy-terminal domain (CTD). The grey box around the RNA helicase and CTD domains indicated that this is the region used for the modelling. **(B)** RIG-1 was screened using the web server DisoLipPred – Disordered Lipid binding Predictor, to predict disordered lipid binding regions (DLBR). A larger value of propensity refers to a higher likelihood of that amino acid residue to be inside a DLBR with a lower value reflecting a lower likelihood that the amino acid residue will be a part of a DLBR. Dotted line is representative of a threshold identified within DisoLipPred software. **(C)** Structural model of viral RNA (blue) in complex with RIG-1 (amino acids 241-922, grey) shows key domains highlighted by colour are Hel 1 (yellow), Hel2 (cyan) and the C-terminus (magenta). Also highlighted by red spheres are the amino acids bioinformatically proposed to interact with the phosphatidylcholine (POPC) lipid bilayer (wheat).

### *The lipid droplet lipidome dynamically changes following activation of antiviral early innate signalling pathways*

Viruses alter the cellular lipidome in a pro-viral manner to enhance their own replication cycles (as reviewed in (*31*)), however, these changes are usually examined at later infection time points, excluding the possibility that early cellular lipid changes may occur to facilitate a pro-host response. It is plausible that changes in lipid composition within the LD itself may assist in both altering the proteome of LDs as well as potentially enhancing the antiviral environment, however a lipidome analysis of LDs following viral infection has not yet been performed at early time points following viral infection prior to viral cellular remodeling. This manuscript has applied a dual-omics approach to better understand the regulation of lipids simultaneously with proteins on the virally driven LD following activation of the cellular early innate antiviral response, which may offer further insight into the role LDs may play during viral infection.

There were limited changes to lipids observed in the whole cell lysates following dsRNA stimulation of astrocyte cells despite the increase in the overall lipid quantity following innate immune activation (Fig S7A), likely driven by the increase in cellular LDs. However, there were significant changes in relative abundance of the four lipid categories examined within the LD lipidome (Fig 7A). Lipid changes within the LDs were seen as early as 8 hrs, with greater changes observed at 24 hrs (Fig S7A, B), towards an increased abundance of glycerolipids, and a decrease in sterols (Fig 7A, Table S4). Further analysis of individual lipid classes was able to detect a total of 491 different lipid species, revealing that following activation of antiviral pathways, LDs generally altered their lipidome to increase the relative abundance of long-chain polyunsaturated triacylglycerols (chain lengths of 13-21 carbons, pink triangle, Fig 7B, Fig S7C, D), whilst decreasing saturated cholesterol esters (blue circles, Fig 7B and Fig S7C). A small but significant change was also observed in the phospholipids making up the LD membrane, with an increase in PE (phosphatidylethanolamine) and PI (phosphatidylinositol) lipids (Fig 7C). Small changes in these membrane phospholipids are known to alter membrane curvature, stability, and their ability to incorporate proteins (*16–20*). There was also an upregulation of ether linkages in these structural lipids between 8 and 24 hrs (Fig 7D), which are known to support membrane functional changes, including cellular signalling at lipid membranes (*32*).

Using our dual omics approach we were able to show that the virally driven LD proteome supported the changes observed across phospholipid and glycerolipid classes, as well as the

observed increases in long chain polyunsaturated fatty acids (PUFAs) (Fig 8A, B, C). Lipid modification enzymes found within our proteome were heavily weighted towards involvement in glycerolipid and phospholipid metabolism (Fig 8B), with high upregulation of the enzymes ACSL1, ACSL3 and ACSL4 (Fig 8A), known to be involved in the synthesis of long-chain fatty acids being observed.

***Long and very-long chain fatty acids within lipid droplets promote an antiviral response***

Virally driven LDs displayed enhanced levels of polyunsaturated triglycerides (Fig 7B), with elongated chain length (Fig S7D). To further understand the abundance of long chain fatty acids in LDs following activation of early innate immune signalling we performed fatty acid chain length analysis across all lipid classes. As can be seen in figure 8D, there is a statistically significant increase in multiple fatty acid chain lengths from the long (>18) and very long (>22) categories present within LDs. These fatty acid changes belonged mainly to the phospholipid and glycerolipid classes, with a general decrease in these fatty acid chain lengths observed in sphingolipids (Fig S8).

The role of individual fatty acids within LDs has not previously been examined, although some of the identified individual fatty acids that are differentially regulated in our data have shown antiviral activity when added to cell cultures *in vitro* (*33–35*). We have recently optimised an artificial lipid droplet (aLD) system that is deliverable to multiple cells types at high levels (*36*). Using this system, we examined the potential of some of the most highly up and down regulated long chain fatty acids within our LDs following viral infection, for their ability to influence viral replication. Fatty acids were chosen from the top 10 regulated fatty acids based on their commercial availability and were incorporated into the neutral lipid component of our aLDs. Notably, the delivery of artificial lipid droplets themselves, composed of a neutral lipid TAG core and a complex phospholipid layer comprising PC, PE and PI, as we have delivered previously (*36*), was able to restrict ZIKV infection *in vitro* (Fig 8E). This also coincided with increases in both type I and III IFN mRNA as well as the downstream ISG, viperin (Fig 8F). Of the 8 long chain fatty acids delivered within our artificial lipid droplets, only 2 of the LD upregulated PUFAs were shown to directly restrict ZIKV replication, arachidonic acid (AA) and eicosapentaenoic acid (EPA), interestingly, delivery of both PUFAs within our aLDs also significantly enhanced the cellular transcription of both type I and III IFNs as well as viperin, indicating that these PUFAs

441 may have a direct contribution to enhancing antiviral cytokine expression (Fig 8E and F). Delivery
442 of the four LD downregulated fatty acids in aLDs to cells, in all instances but one (NA: Nervonic
443 acid) demonstrated a significant increase in ZIKV replication, indicating that these fatty acids may
444 be detrimental to a pro-host environment following viral infection.

# Figure 7.

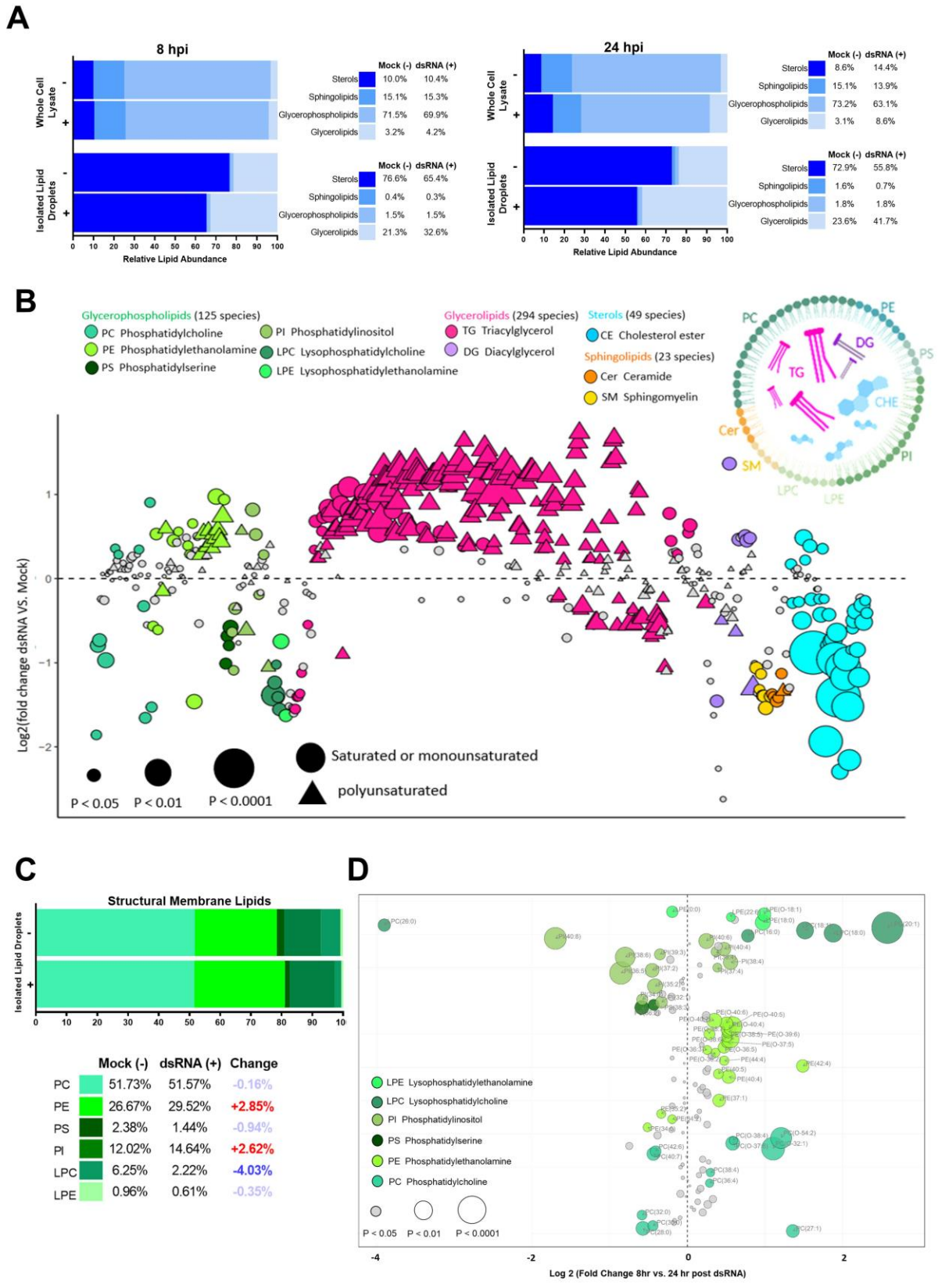
A
8 hpi
24 hpi
Whole Cell Lysate
Isolated Lipid Droplets
Relative Lipid Abundance
Mock (-) dsRNA (+)
Sterols 10.0% 10.4%
Sphingolipids 15.1% 15.3%
Glycerophospholipids 71.5% 69.9%
Glycerolipids 3.2% 4.2%
Sterols 76.6% 65.4%
Sphingolipids 0.4% 0.3%
Glycerophospholipids 1.5% 1.5%
Glycerolipids 21.3% 32.6%
Sterols 8.6% 14.4%
Sphingolipids 15.1% 13.9%
Glycerophospholipids 73.2% 63.1%
Glycerolipids 3.1% 8.6%
Sterols 72.9% 55.8%
Sphingolipids 1.6% 0.7%
Glycerophospholipids 1.8% 1.8%
Glycerolipids 23.6% 41.7%
B
Glycerophospholipids (125 species)
PC Phosphatidylcholine
PE Phosphatidylethanolamine
PS Phosphatidylserine
PI Phosphatidylinositol
LPC Lysophosphatidylcholine
LPE Lysophosphatidylethanolamine
Glycerolipids (294 species)
TG Triacylglycerol
DG Diacylglycerol
Sterols (49 species)
CE Cholesterol ester
Sphingolipids (23 species)
Cer Ceramide
SM Sphingomyelin
Log2(fold change dsRNA VS. Mock)
Saturated or monounsaturated
polyunsaturated
P < 0.05
P < 0.01
P < 0.0001
C
Structural Membrane Lipids
Isolated Lipid Droplets
Mock (-) dsRNA (+) Change
PC 51.73% 51.57% -0.16%
PE 26.67% 29.52% +2.85%
PS 2.38% 1.44% -0.94%
PI 12.02% 14.64% +2.62%
LPC 6.25% 2.22% -4.03%
LPE 0.96% 0.61% -0.35%
D
LPE Lysophosphatidylethanolamine
LPC Lysophosphatidylcholine
PI Phosphatidylinositol
PS Phosphatidylserine
PE Phosphatidylethanolamine
PC Phosphatidylcholine
P < 0.05
P < 0.01
P < 0.0001
Log 2 (Fold Change 8hr vs. 24 hr post dsRNA)

445

**Fig. 7. The lipidome of lipid droplets changes significantly following dsRNA stimulation in primary immortalised astrocytes. (A)** The relative abundance of major lipid categories (Glycerolipids, Glycerophospholipids, Sphingolipids and Sterols) in following groups; whole cell lysate post dsRNA stimulation at 8 and 24 hrs, LD fractions post dsRNA stimulation at 8 and 24 hrs. **(B)** Bubble plot of log2 fold changes in abundance of individual lipid species post dsRNA stimulation relative to mock at 24 hrs. Significance was determined by unpaired two-tailed students *t* test (n=3). Individual lipid species are coloured by the class of lipid that they belong to. PC phosphatidylcholine; PE phosphatidylethanolamine; PI phosphatidylinositol; PS phosphatidylserine; LPC lysophosphatidylcholine; LPE lysophosphatidylethanolamine; DAG diacylglycerol; TAG triacylglycerol; Cer ceramide; SM sphingomyelin; CE cholesterol ester. **(C)** Changes in relative abundance of membrane phospholipids (PC phosphatidylcholine; PE phosphatidylethanolamine; PI phosphatidylinositol; PS phosphatidylserine; LPC lysophosphatidylcholine; LPE lysophosphatidylethanolamine) following dsRNA stimulation at 24 hrs in isolated LDs. **(D)** Bubble plot of log2 fold changes in relative abundance membrane phospholipids in isolated LDs following dsRNA stimulation from 8 hrs to 24 hrs. Individual phospholipid species (PC phosphatidylcholine; PE phosphatidylethanolamine; PI phosphatidylinositol; PS phosphatidylserine; LPC lysophosphatidylcholine; LPE lysophosphatidylethanolamine) characterized by abundance in LDs at 8 hrs relative to LDs at 24 hrs post dsRNA stimulation. Significance was determined by unpaired two-tailed students *t* test (n = 3).

## Figure 8.

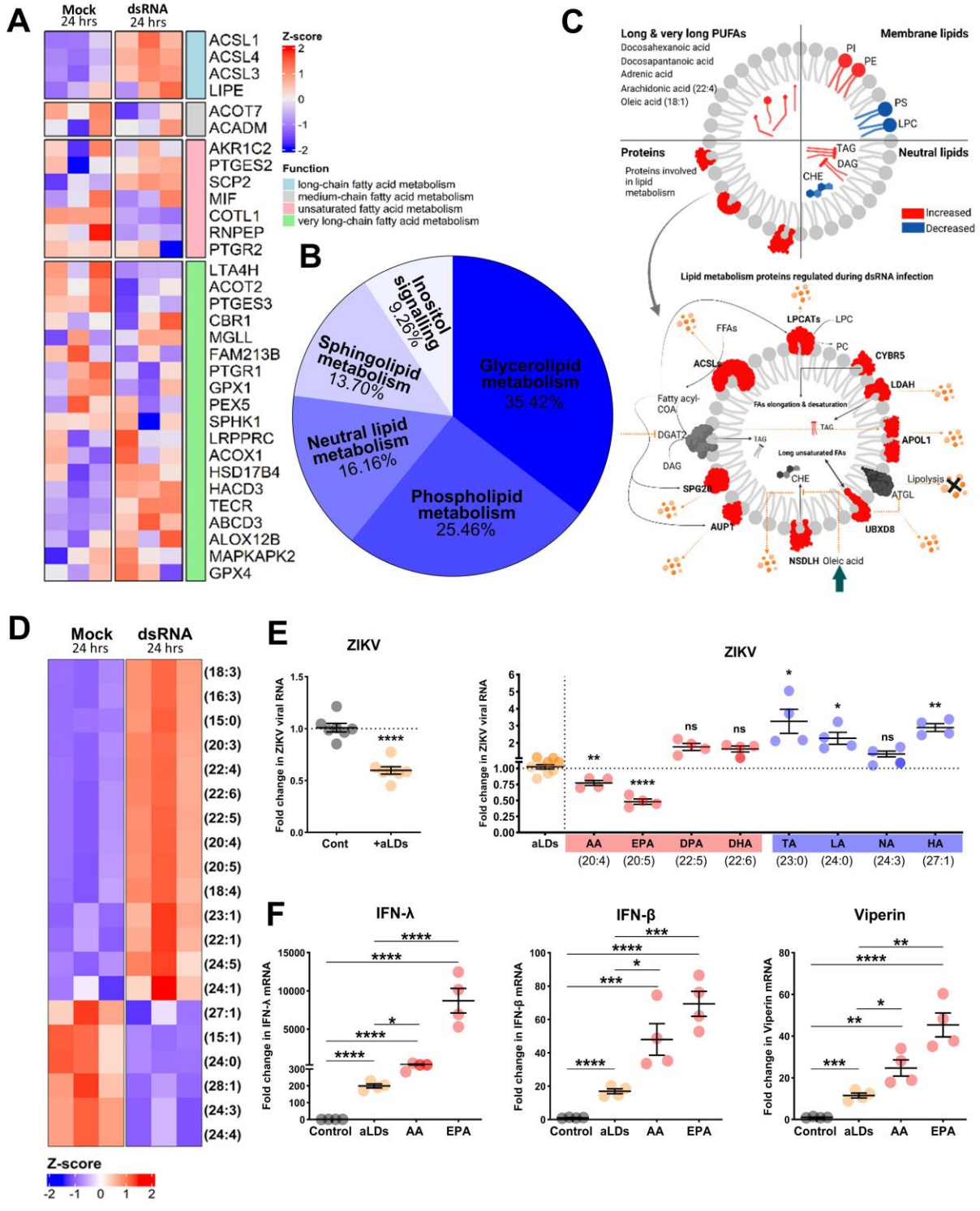
A
Mock 24 hrs
dsRNA 24 hrs
Z-score
2
1
0
-1
-2
ACSL1
ACSL4
ACSL3
LIPE
ACOT7
ACADM
AKR1C2
PTGES2
SCP2
MIF
COTL1
RNPEP
PTGR2
LTA4H
ACOT2
PTGES3
CBR1
MGLL
FAM213B
PTGR1
GPX1
PEX5
SPHK1
LRPPRC
ACOX1
HSD17B4
HACD3
TECR
ABCD3
ALOX12B
MAPKAPK2
GPX4
Function
long-chain fatty acid metabolism
medium-chain fatty acid metabolism
unsaturated fatty acid metabolism
very long-chain fatty acid metabolism
B
Inositol signalling 9.26%
Sphingolipid metabolism 13.70%
Glycerolipid metabolism 35.42%
Neutral lipid metabolism 16.16%
Phospholipid metabolism 25.46%
C
Long & very long PUFAs
Docosahexanoic acid
Docosapantanoic acid
Adrenic acid
Arachidonic acid (22:4)
Oleic acid (18:1)
Membrane lipids
PI
PE
PS
LPC
Proteins
Proteins involved in lipid metabolism
TAG
DAG
CHE
Neutral lipids
Increased
Decreased
Lipid metabolism proteins regulated during dsRNA infection
FFAs
LPCATs
LPC
PC
CYBR5
ACSL
LDAH
Fatty acyl-COA
FAs elongation & desaturation
TAG
DGAT2
APOL1
DAG
Long unsaturated FAs
CHE
Lipolysis
ATGL
SPG20
AUP1
UBXD8
NSDLH
Oleic acid
D
Mock 24 hrs
dsRNA 24 hrs
(18:3)
(16:3)
(15:0)
(20:3)
(22:4)
(22:6)
(22:5)
(20:4)
(20:5)
(18:4)
(23:1)
(22:1)
(24:5)
(24:1)
(27:1)
(15:1)
(24:0)
(28:1)
(24:3)
(24:4)
Z-score
-2 -1 0 1 2
E
ZIKV
Fold change in ZIKV viral RNA
Cont
+aLDs
ZIKV
aLDs
AA (20:4)
EPA (20:5)
DPA (22:5)
DHA (22:6)
TA (23:0)
LA (24:0)
NA (24:3)
HA (27:1)
F
IFN-λ
Fold change in IFN-λ mRNA
IFN-β
Fold change in IFN-β mRNA
Viperin
Fold change in Viperin mRNA
Control
aLDs
AA
EPA

467

**Fig 8. Long-chain fatty acids upregulated in lipid droplets during infection are antiviral. (A and B)** Distribution of identified LD resident proteins involved in lipid metabolism post dsRNA stimulation at 24 hrs based on the percentage abundance. Gene ontology was performed using the Uniprot database within Perseus. Proteins were grouped into 4 main categories (involved in regulating fatty acids metabolism). **(C)** Schematic of the lipidomic and related proteomic changes in LDs following infection. Overview of changes in LD's lipidome complemented by upregulation of LD`s proteins involved in lipid metabolism. Proteins involved in lipid metabolism (long/very long/ poly unsaturated fatty acids (PUFAs) metabolism) were identified as significantly upregulated post dsRNA stimulation. These proteins could potentially play roles in LDs accumulation and protein recruitment to LDs (SPG20 & AUP1), fatty acids elongation and poly unsaturation (e.g., ACSLs, CYBR5 & UBXD8), increase in Triglycerides (e.g., APOL1 & LDAH), decrease in cholesterol esters (e.g., NSDHL) & also phospholipid synthesis (e.g., LPCAT), which were the main alterations observed in LDs lipidomic profile post dsRNA stimulation in primary immortalised astrocytes at 24 hrs. **(D)** Heatmap displaying z-score of significantly changed LD's fatty acids with highest and lowest log2 fold change in dsRNA stimulated primary immortalized astrocytes; Blue tiles refer to fatty acids with a z-score < 0 with red tiles referring to fatty acids with a z-score > 0. **(E and F)** Primary immortalised astrocyte cells were infected with ZIKV (MOI 1) for 4 h prior to treatment with 100,000 aLDs/cell containing the top up/down regulated fatty acids for 16 h. RT-qPCR was performed to evaluate ZIKV, IFN-β, IFN-λ and viperin mRNA expression. All results are in comparison to RPLP0 expression. Error bars, mean values ± SEM, P values were determined by unpaired two-tailed Student's t test with a Holm-Sidak correction for multiple comparisons for 2 or more groups. Stimulated cells were statistically compared with their respective mock controls, ns = not significant. ($n = 4$ biological replicates).

# Discussion

The role of LDs in viral infection has been predominantly studied from a pro-viral point of view, where some viruses usurp the LD as a platform for assembly by manipulating its lipolysis and biogenesis to help enhance the viral life cycle (*8*). However, recent research has demonstrated that LD numbers rapidly increase during early viral infection via an EGFR dependant mechanism (*10*). This pathway is distinct from the homeostatic turnover of LDs and is essential for the optimal production of antiviral cytokines (*10*), highlighting LDs as critical organelles in mounting an effective antiviral immune response. LDs are the main lipid storage organelle of the cell, and although the lipidome of the whole cell has been extensively studied during viral infection (*37–40*), lipidomic changes occurring within the LD is yet to be examined. Here we use a powerful dual-omics approach to examine the proteomic and lipidomic changes of virally induced LDs in astrocyte cells, the main producers of LDs in the brain, to dissect the role they play in generating an antiviral host cell environment.

We found that the astrocyte LD proteome undergoes dynamic changes following viral infection, enhancing the presence of antiviral and signalling proteins. This included the recruitment of directly antiviral proteins such as IFIT1 and IFIT2, two ISGs known to bind viral RNA species and inhibit their translation (*41–43*). Additionally, RSAD2 (viperin), a protein that both directly restricts RNA viruses and enhances antiviral signalling through signalosome formation, was upregulated following infection (*14*, *44*, *45*). Signalosome formation is a requirement for efficient signalling intracellularly, to increase local concentrations of signalling components and promote weak interactions that may be required for enzyme activation. This process typically occurs at specific membrane platforms such as the ER for STING, the mitochondria and peroxisome for MAVS, and more recently, endosomes which transiently accumulate RIG-I to facilitate poly-ubiquitylation (*13*, *46*, *47*). Alternatively, signalling molecules like cGAS can form self-organising centres to concentrate their reactions (*15*). Here, we demonstrate that LDs serve as a platform for localising key signalling proteins required for the production of both type I interferons and ISGs: critical components of the antiviral response. While some of these proteins remain constant at the LD surface (MDA5, STAT2), others accumulated transiently following viral infection (RIG-I, STAT1). As previously described, LD biogenesis in this context is driven by a non-homeostatic, EGFR-dependent mechanism (*10*), and we demonstrate that STAT1 localisation to LDs was specific to virally driven LDs, not those formed under homeostatic conditions.

Ultimately, transient localisation of proteins to the LD surface is not well understood, however, post-translational modifications (PTMs) are hypothesied to play a key role. Supporting this, approximately 8.4% of the LD proteome following innate immune activation comprised enzymes involved in PTMs (Fig S9A, and as reviewed in (*6*)).

In addition to proteomic changes, we observed alterations in the LD lipidome that may contribute to protein recruitment. Specifically, the external phospholipid membrane composition shifted towards a profile known to enhance membrane curvature, protein binding capacity and cellular signalling at lipid membranes (*19*, *48–55*). These structural changes were accompanied by large alterations in the neutral lipid content, with a shift towards long-chain fatty acids, including antiviral lipids previously shown to impair viral replication (*33–35*). Our dual-omics approach revealed that enzymatic proteomic changes observed in the LD proteome likely drive these lipidomic alterations. Notable proteomic changes included increased expression of enzymes involved in fatty acid elongation and poly-unsaturation (e.g., ACSLs, CYBR5, UBXD8), triglyceride synthesis (e.g., APOL1, LDAH), and phospholipid modification (e.g., LPCAT), alongside reduced expression of cholesterol ester synthesis proteins (e.g., NSDHL). These findings highlight the power of a dual-omics strategy in elucidating the coordinated molecular changes that occur on LDs during viral infection.

The antiviral roles of lipids remain relatively understudied, particularly given the vast diversity of lipid species. Notably, the specific functions of lipids within the LD itself have not previously been explored. Recently, interest has grown in the role of bioactive lipid mediators during viral infection (*8*), many of which are synthesised by LD-localised enzymes to generate a diverse array of signalling molecules. Eicosanoids represent a major class of these bioactive lipids, and many of the fatty acids upregulated in LDs following viral infection are known eicosanoid precursors. The delivery of two of these fatty acids (arachidonic acid and eicosapentaenoic acid) using an artificial lipid droplet delivery system was able to significantly decrease ZIKV replication *in vitro*. While the delivery of other enriched fatty acids such as docosapentaenoic acid (DPA) and docosahexaenoic acid (DHA) within aLDs did not directly affect viral replication, it is plausible that they may have an in-direct overall pro-host antiviral response within the cell, and future work will need to be performed to assess this. Polyunsaturated fatty acids (PUFAs) such as arachidonic acid (AA) and eicosapentaenoic acid (EPA) have previously been shown to inhibit multiple enveloped viruses, including ZIKV infection (*33*, *56*, *57*), primarily through interference with early

stages of the viral life cycle (e.g., attachment, fusion, or entry). Here we demonstrate a previously undescribed antiviral mechanisms for these LD-localised PUFAs, where they are able to act from within the LD to drive significant upregulation of antiviral interferons and ISG mRNAs. Lastly, it cannot be overlooked that cellular lipids are in a constant flux, and fatty acids stored in LDs are frequently mobilised to generate new lipids for cellular functions. Thus, the rapid lipidomic changes observed in virally induced LDs may support broader metabolic reprogramming and signalling required during infection.

Although LD proteomes are understood to be dynamic in nature, the mechanisms underlying these changes remain poorly defined due to limited proteomic datasets (*58*, *59*). The LD proteome has previous been shown to be highly sensitive to bacterial LPS stimulation (*11*), however, we observed only a 17-protein overlap between LPS-induced and viral RNA-induced LD proteomic changes, suggesting a pathogen-specific reprogramming of the LD proteome (Fig S9B S9C). Shared proteins were primarily involved in organelle trafficking and lipid metabolism, implying a core function of LDs in pathogen response: trafficking through the cell and modulating lipid species. (Fig S9C). To our knowledge this is the first study to apply a dual-omics approach to concurrently analyse the changing LD proteome and lipidome in mammalian cells. This powerful tool enabled us to associate changes in metabolic enzymes in the LD proteome with changes seen in both the increases of lipids having long-chain fatty acyl chains, and the smaller alterations observed in the structural lipids of the LD membrane. Our approach also highlighted the striking presence of multiple enzymes involved in post-translational modification of proteins, and potentially lipids within the LD proteome. These findings support a model in which virally induced LDs not only coordinate protein localisation for antiviral signalling, but also drive the synthesis of bioactive lipid mediators, such as eicosanoids, that contribute to the cellular immune defence (*8*, *17*, *18*, *60*, *61*).

LDs are rapidly upregulated following viral infection by non-homeostatic mechanisms and are critical in the early innate immune response facilitating a heightened antiviral environment (*10*). These studies highlight that viral driven LD upregulation coincides with dynamic changes to the LD lipidome and proteome to facilitate antiviral signalosome formation and the production of antiviral lipid species. Understanding these mechanisms may enable the development of next-generation antiviral strategies that enhance host cell immunity in a broad, pathogen-agnostic manner.

**Acknowledgments:** We acknowledge that the bulk of this project was conducted on the traditional homelands of the Wurundjeri Woi wurrung people. We would like to thank the La Trobe University Bioimaging Facility for their assistance with image acquisition, data collection and image analysis essential to this work. We also acknowledge the use of the Bio21 Mass Spectrometry and Proteomics Facility at the University of Melbourne and thank them for their continued support of our projects. We would like to thank Associate Professor Greg Mosely from Monash University (Melbourne, Australia) for gifting us the STAT1 and 2 mCherry constructs, Professor Stephen Polyak from the University of Washington (Seattle, WA) for gifting us the RIG-I-wt construct and Prof Paul Herzog from the Hudson Institute (Melbourne, Australia) for gifting us the MAVS antibody. All schematic diagrams throughout this manuscript were created using BioRender.

**Funding:** National Health and Medical Research Council New Ideas Grant APP1181434 (KJH, DRW) and APP2038548 (KJH, AM). National Health and Medical Research Council Investigator Grant APP2033787 (EAM). Australian Research Council Discovery Early Career Research Award DE200100584 (DRW). CASS foundation Medicine/Science grant (EAM). Jack Brockhoff Foundation Medical grant (EAM). Holsworth Biomedical Research Initiative under the auspices of the Bendigo Tertiary Education Anniversary Foundation (DRW AJM, AMR). La Trobe University Internal funding schemes (EAM, KJH)

**Author contributions:** Conceptualization: EAM, KJH. Methodology: EAM, SN, NW, JLL, MLS, ZT, CJ, AJM, AMR, DRW, KJH. Investigation: EAM, JLL, ZT, AJM, AMR, IA, MLS, VT, QD, CJ, MJH, SN, KJH. Visualization: EAM, JLL, ZT, AJM, AMR, IA, CJ, SN, DRW, KJH. Funding acquisition: EAM, AJM, AMR, DRW, KJH. Project administration: EAM, KJH, DRW. Supervision: EAM, DRW, KJH. Writing – original draft: EAM, KJH. Writing – review & editing: EAM, ZT, JLL, IA, AJM, DRW, SN, KJH. All authors participated in reviewing and editing the manuscript.

**Competing interests:** Authors declare that they have no competing interests.

**Data and materials availability:** All data is available in the main text, or the supplementary materials provided.

**Supplementary Materials**

Figs. S1 to S7
Tables S1 to S4
Movies S1 to S4

# Materials and Methods

## Cells and culture conditions

Primary Immortalised Human Fetal Astrocytes were used throughout this study (referred to as primary immortalised astrocyte cells). These cells were maintained at 37 °C in a 5% $CO_2$ air atmosphere in DMEM (Gibco, Cat; 12430054) containing 10% fetal bovine serum (FBS) (Gibco,

Cat; 10099141), 100 units/mL penicillin and 100 µg/mL streptomycin (Sigma-Aldrich, cat; P0781).

**Lymphocytic Choriomeningitis Virus (LCMV) infection of mice**

C57BL/6 mice were obtained from Australian BioResources (Moss Vale, NSW 2577) and housed under specific pathogen–free conditions in the animal facility at the University of Sydney, Sydney, Australia. Animal experiments were performed in accordance with the University of Sydney's Animal Ethics Committee (1738/2020) and Institutional Biosafety Committee approval NLRD (22N004); mice were maintained under a 12 hr light/dark cycle at an ambient temperature of 20–23 °C and relative humidity of 40–60% and with ample food and water. All experiments were done in accordance with the Institutional Animal Care and Use Committee guidelines of the University of Sydney. All mice were aged between 8 and 16 weeks at the time of infection. Mice were anesthetized with 100 µg ketamine and 1 µg xylazine per gram bodyweight and intracranial infection was performed by injecting 500 PFU of LCMV (strain LCMV Armstrong 53b) diluted in 20 µL of phosphate-buffered saline (PBS) with 1% fetal bovine serum (FBS). Sham-infected mice were used as controls and received the same volume of PBS with 1% FBS but without virus. Mice were weighed at the times indicated below, and percent weight change was calculated. Mice were euthanized at 2- or 4-days post infection, and the brains were removed, flash frozen in optimum cutting temperature (OCT) medium.

***In vitro* viral infection, viral mimics stimulation and plasmid transfection**

Primary immortalised astrocyte cells were seeded at $5x10^6$ per T175cm$^2$ flask plates prior to infection with Zika virus (MR766 strain) at an MOI of 1. Cells were washed once with PBS then infected with virus in serum free media for 4 hrs, followed by 20 hrs in DMEM supplemented with 10% fetal calf serum, at 37 °C containing 5% $CO_2$. The viral mimic, poly I:C (dsRNA) (Invivogen) and all plasmid constructs used throughout the study were transfected into cells using PEI transfection reagent (Polyscience, Cat; 24765-1) at a concentration of 1 µg/ml. Viperin-mCherry and control mCherry plasmids were created as described previously (*62*). STAT1- and STAT2-mCherry tagged plasmids were kindly gifted to us from Associate Professor Greg Mosely (Monash University, Melbourne, VIC). RIG-I-wt was kindly gifted to us from Professor Stephen Polyak (University of Washington, Seattle, WA).

**Immunofluorescence microscopy**

For cultured cells, briefly, cells were grown in 24-well plates on 12 mm glass coverslips coated with gelatine (0.2% [v/v]) were washed with PBS, fixed with 4% paraformaldehyde in PBS for 15 min at room temperature and permeabilised with 0.1% Triton X-100 in PBS for 10 min. Cells were blocked with 5% BSA for 1 hr, before antibody staining with αRIG-I (1:200; MA5-31715, Thermo Fisher Scientific), αMAVS (1:100; PA5-17256, Thermo Fisher Scientific). Cells were then incubated with Alexa Fluor 647 (1:200; A21236, Thermo Fisher) or Alexa Fluor 488 (1:200; A11008, Thermo Fisher Scientific) secondary antibody for 1 hr. Mitochondria were stained by incubating live cells with MitoTracker® Red (Thermo Fisher Scientific) at 100nM for 1 hr. LDs were stained by incubating cells with Bodipy (493/503) at 1 ng/mL for 1 hr and nuclei were stained with DAPI (Sigma-Aldrich, 1 µg/ml) for 5 min at room temperature. Samples were then washed with PBS and mounted with Vectashield Antifade Mounting Medium (Vector Laboratories). Preparation and staining of murine frozen brain sections were prepared following optimised protocols for tissue sections (*63*). Whole brains were sectioned sagittally. One section was snap-frozen and the other mounted immediately in OCT. Frozen sections were cut at 14 µM with a Leica

CM 3050 S cryostat and mounted on microscope slides and stored at −80 °C. Sections were fixed with 4% paraformaldehyde in PBS for 15 min at room temperature. Sections were then washed with PBS, permeabilised with 0.1% Triton X-100 in PBS for 10 min, washed again and then blocked with 1% BSA for 30 mins. Sections were stained for specific cell types; astrocytes (αGFAP polyclonal antibody, 1:1000; PA3-16727, Invitrogen), neurons (αNeuN polyclonal antibody, 1:2500; PA5-78639, Invitrogen) and microglia (αTMEM119 monoclonal antibody, 1:10000; MA5-35043, Invitrogen). Sections were then washed and incubated with Alexa Fluor 555 secondary antibody at 1:200 for 1 hr. Bodipy (493/503) was used to stain for LDs at 1 ng/mL for 1 hr at room temperature, and nuclei were stained with DAPI for 5 min at room temperature. Images were then acquired using a Zeiss 800 confocal microscope. Unless otherwise indicated images were processed using ImageJ analysis software.

**Lipid Droplet Isolation**

Isolation of LD from cells and brain tissues was performed using a Lipid Droplet Isolation Kit (Cell Biolabs; Cat; MET-5011). For cells, 5x T-175cm$^2$ flasks (5 x 106 cells) of primary immortalised astrocyte cells were trypsinised, pelleted at 1000 g for 5 mins, washed 2 times with 1 x PBS. Mouse brain tissues were thawed on ice and 200mg of tissue surrounding the hippocampus was minced and put into sterile 1.5 mL microcentrifuge tube. Both cells and tissues were resuspended in 200 µl of reagent A (Cell Biolabs; Cat; MET-5011) and incubated on ice for 10 mins with occasional vortexing. 800 µl of 1 x reagent B (Cell Biolabs; Cat; MET-5011) was added to the cells/ tissues and further incubated on ice for 10 mins with occasional vortexing. Following incubation, cells/ tissues were carefully homogenised by being passed through a one inch 27-gauge needle attached to a 3 mL syringe five times. 600 µl of 1x reagent B was layered on top of the homogenates. Lysates were centrifuged for 3 hrs at 20,000 g at 4 °C. 100 µL of the top layer containing the floating LDs was taken per condition and either stored at −80 °C for omic analysis of proteins and lipids or used for purity testing via western blot.

**Visualisation and analysis of mCherry co-localisation to isolated lipid droplets**

Primary immortalised astrocytes were seeded at 5x10$^6$ per T175cm$^2$ flask prior to transfection with mCherry, viperin-mCherry, STAT1-mCherry and STAT2-mCherry. Cells were trypsinised and LDs were isolated. Following LD isolation, LDs were stained with Bodipy (493/503) at a concentration of 1 ng/mL. 10uls of purified LDs were spotted on a Nunc Lab-Tek II Chamber Slide System (Thermo Fisher Scientific) and were visualised via a Zeiss LSM 780 high-sensitivity laser scanning confocal microscope at 63x to determine both LDs stained with Bodipy (493/503) and mCherry expressing protein co-localisation. Image analysis was carried out using ImageJ, with LDs segmented using the Find Maxima function and a segmentation map was created. Segmentation maps were then used to separate interacting LDs and the Particle Analyser plugin was used to count LDs, create ROIs, and determine their sizes. To determine which LDs contained protein the LD area was isolated using an intensity threshold, and a binary image was created. The same method was used to find areas containing protein. The areas where both binaries overlapped was then determined via image calculator. This mask was then used in combination with the created ROIs to determine the presence or absence of protein in each LD.

**SMLM Image Acquisition and Processing**

Switching buffer was applied to cells containing 80 µL 1M mercaptoethylamine (MEA), 20 µL 1 M potassium hydroxide (KOH) and 0.8 µL 1 mg/mL Bodipy (493/503) in PBS (pH 8.5) immediately prior to imaging. 8-well chamber slides were mounted on a custom SMLM setup

based on (*64*). Briefly, the setup is built around an Olympus IX-83 inverted fluorescence microscope equipped with a 100X 1.49 oil immersion objective and a Photometrics Prime-95B sCMOS detector coupled to a pair of excitation lasers using appropriate dichroics and focal lenses (Semrock, Thorlabs). Diffraction-limited epifluorescence images of LDs were captured using 488 nm excitation at 8 mW (200 mW, Cobalt MLD), with 40 ms exposure. SMLM images were constructed by capturing 10,000 frames at 100 Hz with 200 mW 640 nm excitation (iBeam Smart, Toptica).

**SMLM Image Acquisition and Processing**

Switching buffer was applied to cells containing 80 µL 1 M mercaptoethylamine (MEA), 20 µL 1 M potassium hydroxide (KOH) and 0.8 µL 1 mg/mL Bodipy (493/503) in 1x PBS (pH 8.5) immediately prior to imaging. 8-well chamber slides were mounted on a custom SMLM setup based on (*64*). Briefly, the setup is built around an Olympus IX-83 inverted fluorescence microscope equipped with a 100X 1.49 oil immersion objective and a Photometrics Prime-95B sCMOS detector coupled to a pair of excitation lasers using appropriate dichroics and focal lenses (Semrock, Thorlabs). Diffraction-limited epifluorescence images of LDs were captured using 488 nm excitation at 8 mW (200 mW, Cobalt MLD), with 40 ms exposure. SMLM images were constructed by capturing 10,000 frames at 100 Hz with 200 mW 640 nm excitation and 10 ms exposure (iBeam Smart, Toptica).

**Cytoplasmic lipid droplet Co-localisation Enumeration**

*Confocal image analysis:* For each condition, at least 9 cells were imaged at 60X magnification from varying locations of the coverslip and were deconvoluted prior to analysis. Images were imported into Imaris (v9.5) with transfected cells isolated and masked to create a region of interest for co-localisation analysis. Co-localisation analysis was performed within Imaris using the auto threshold option comparing LDs and mCherry tagged proteins. Manders A Coefficient values were used to quantify co-localisation of mCherry tagged proteins to LDs.

*Super resolution image analysis:* For each time point, at least 10 fields of view were imaged at 100X magnification from varying locations across each well of the chamber slides. Images were imported to FIJI (ImageJ) and the LD channel converted to 16-bit before being scaled to 3000x3000, smoothed and binarized. The STAT channel was analysed using the ThunderSTORM plugin for FIJI to determine molecular coordinates from raw TIFF stacks and normalised gaussian renderings. These images were converted to 16-bit, smoothed and binarized before being overlayed with the LD channel to form the final merged LD-STAT images. To determine the number of colocalisations per cell, images were further analysed using the interaction factor analysis plugin which is specifically designed to assess dense SMLM data and normalizes for coincidental co-localisation by generating Monte Carlo-based random renderings. This analysis was used to generate a ratio of real co-localisation to the number expected if only random interactions were present such that a ratio of 1 indicates entirely random overlap, where 2 indicates twice as many interactions as randomly modelled. These ratios are referred to throughout as 'co-localisation coefficient'. Number of co-localisations for each image were determined using this object co-localisation analysis plugin of ImageJ.

**Western Blotting**

Lysates were subjected to SDS-PAGE. The proteins were transferred to 0.2 µm nitrocellulose membranes (Bio-Strategy, Campbellfield, VIC, Australia) and probed with primary antibodies. The primary antibodies used were: mouse monoclonal αCalnexin (1:1000; sc-23954, Santa Cruz

Biotechnology), mouse monoclonal αmfn1 (1:1000; sc-166644, Santa Cruz Biotechnology), mouse monoclonal αACOX1 (1:1000; sc-517306, Santa Cruz Biotechnology), rabbit monoclonal αPerilipin-2 (1:2000; ab108323, Abcam), mouse monoclonal αRIG-I (1:1000; sc-376845 Santa Cruz Biotechnology), rabbit monoclonal αMX1 (1:2000; ab207414, Abcam), rabbit polyclonal αSTAT1 (1:1000; 9172, Cell Signaling Technology), rabbit monoclonal αSTAT2 (1:1000; A3588, ABclonal), rabbit polyclonal αZC3HAV1 (1:5000; ab154680, Abcam), rabbit monoclonal αPhospho-STAT1 (Tyr701) (1:1000; #7649, Cell Signaling Technology), rabbit polyclonal αmCherry (1:1000; 5993, BioVision) and rabbit polyclonal αTRIM25 (1:1000; ab86365, Abcam). To probe for ZIKV antigen, mouse α4G2 hybridoma fluid against flavivirus group antigen was used in a 1:1 ratio with 5% skim milk. Following 3 x 5 min washes with TBS wash buffer, the membrane was incubated with HRP conjugated secondary antibodies (Goat αMouse IgG (H+L) Secondary Antibody, HRP, 31430, Thermo Fisher Scientific) and (Goat αRabbit IgG (H+L) Secondary Antibody, HRP, 31460, Thermo Fisher Scientific) for 1 hr diluted 1:10000. Following 5 x 10 min washes with TBS wash buffer, the membrane was incubated with GE (Amersham) or Femto (Thermo-scientific) Western Developer Reagent, dependent on the required sensitivity. The membranes were scanned using Amersham 600 chemiluminescence imager.

**RNA extraction and real time PCR**

*In vitro* RT-qPCR experiments to evaluate ZIKV replication and IFN expression were performed in 24-well plates with astrocyte cells seeded at $4.5 \times 10^4$/well 24 h prior to infection with ZIKV (MOI 0.1) and treatment with artificial lipid droplets spiked with individual fatty acids. All experiments were performed at least in triplicate. *In vivo* RT-qPCR experiments to evaluate LCMV replication (targeting the nuclear protein) and activation of immune pathways was performed in triplicate from the brain tissue of culled mice used in the omic studies. For all RT-qPCR experiments, total RNA was extracted from cells using TriSure reagent (Bioline), with first strand cDNA being synthesised from total RNA and reverse transcribed using a Tetro cDNA synthesis kit (Bioline). Quantitative real-time PCR was performed in a CFX Connect Real-Time Detection System (BioRad) to quantitate target gene mRNA in comparison to the housekeeping gene RPLPO. Primers sequences can be found in Table 1.

**Table 1: Primer sequences**

| Primer name | Sequence |
|---|---|
| RPLOP0-FP | 5'-AGA TGC AGC AGA TCC GCA T-3' |
| RPLP0-RP | 5'-GGA TGG CCT TGC GCA-3' |
| LCMV(NP)-FP | 5'-CAGAAATGTTGATGCTGGACTGC-3' |
| LCMV(NP)-RP | 5'-CAGACCTTGGCTTGCTTTACACAG-3' |
| ZIKV-FP | 5'CAG CTG GCA TCA TGA AGA AGA AYC-3' |
| ZIKV-RP | 5'CAC YTG TCC CAT CTT YTT CTC C-3' |
| IFN-β-FP | 5'-AGA AAG GAC GAA CAT TGG GAA A-3' |
| IFN-β-RP | 5'-TAG CAG AGC CCT TTT TGA TAA TGT AA-3' |
| IFN-λ -FP | 5'-GAA GAG TCA CTC AAG CTG AAA AAC-3' |
| IFN-λ-RP | 5'-AGA AGC CTC AGG TCC CAA TTC-3' |
| Viperin-FP | 5'GTG AGC AAT GGA AGC CTG ATC-3' |
| Viperin-RP | 5'-GCT GTC ACA GGA GAT AGC GAG AA-3' |

**Protein sample preparation for mass spectrometry**

Proteins samples were precipitated from isolated LDs and whole cell via the S-trap micro protocol. Briefly 70 µl 2x lysis buffer (10% SDS in 50 mM TEAB) to 70 µl liquid sample [at a 1:1 ratio] so that final SDS is 5%. Samples were then sonicated for 5 mins to recover absorbed protein. Samples were then centrifuged for 8 mins at 13,000g. 500mM TCEP was added so that final concentration is 10 mM TCEP and incubate at 55 °C for 15 mins to reduce thiol groups. 500 mM IAA was added to reach final 50 mM IAA and incubate at RT for 30 mins to alkylate disulphides. 27.5% $H_2PO_4$ was then added so that the concentration is ~2.5% phosphoric acid. Samples were vortexed and had pH checked to ensure acidity. 6X binding/wash buffer (100mM TEAB in 90% MeOH) was added to sample and mixed. Samples were centrifuged through the S-trap column at 4,000g for 30 secs to trap proteins. Protein was then cleaned by adding 150 µl of binding/washing buffer, and centrifuged 3 x at 4,000g for 30 secs discarding flowthrough. S-Trap column was then centrifuged at 4,000g for 1 min to fully remove binding/wash buffer. Protein was digested by adding 20 µl of digestion buffer (50mM TEAB + 1 µg Trypsin per 50 µg protein) and incubated at 37°C overnight. Proteins were eluted by adding 40 µl of 50 mM TEAB in water to the S-Trap and incubated for 30 mins. 40 µl of 0.2% formic acid in water was added to the S-Trap followed by centrifugation at 4,000g for 1 min. 40 µl of 50% acetonitrile (ACN) was added to the S-Trap and centrifuged at 4,000g for 1 min. Sample was placed in speedy vac to remove ACN and was followed by freeze drying the sample overnight.

**Lipid Extraction**

Lipids were purified according to a modified protocol (*65*). Briefly, 10 µl of SPLASH Lipidomix (Avanti Polar Lipids) was spiked in each sample as internal standards. Lipids from the whole cell lysates and LD fractions were extracted by diluting lysates with methanol (with 0.01% BHT) so that the final concentration of the sample was 60% v/v MeOH containing 0.01% BHT. Lysates were further diluted with MeOH and $ChCl_3$ so ratio of total H2O:$CHCl_3$: MeOH was 0.74:1:2 and lysates were centrifuged at 14,000 x g for 15 mins to separate phases. Supernatants were collected and dried via speedvac centrifugation prior to analysis via LC-MS/MS.

**Quantitative proteomics and functional annotation analyses**

Proteins were identified by mass spectrometry and relatively quantified by a liquid chromatography approach. Peptide samples were analysed by LC-MS/MS using an Ultimate 3000 UHPLC coupled to an Orbitrap Elite mass spectrometer (Thermo Fisher Scientific, San Jose, CA). Solvent A is 0.1% formic acid (FA) / 5% dimethyl sulfoxide (DMSO) in water and solvent B is 0.1% FA / 5% DMSO in acetonitrile (ACN). Each sample was injected onto a PepMap C18 trap column (75 µM X 2 cm, 3 µM, 100 Å, Thermo Fisher Scientific, San Jose, CA) at 5 µL/min for 6 min using 0.05% trifluoroacetic acid (TFA) / 3% ACN in water and then separated through a PepMap C18 analytical column (75 µM X 50 cm, 2 µM, 100 Å, Thermo Fisher Scientific, San Jose, CA) at a flow rate of 300 nL/min. The temperature of both columns was maintained at 50°C. During separation, the percentage of solvent B in mobile phase was increased from 3% to 23% in 89 min, from 23% to 40% in 10 min and from 40% to 80% in 5 min. Then the columns were cleaned at 80% solvent B for 5 min before decreasing the % B to 3% in 1 min and re-equilibrating for 8 min. The spray voltage, temperature of ion transfer tube and S-lens of the Orbitrap Elite mass spectrometer were set at 1.9 kV, 275 °C and 60% respectively. The full MS scans were acquired at m/z 300 – 1650, a resolving power of 120,000 at m/z 200, an auto gain control (AGC) target value of 1.0 × 106 and a maximum injection time of 200 ms. The top 20 most abundant ions in the MS spectra were subjected to linear ion trap rapid collision induced dissociation (CID) at q value of 0.25, AGC target value of $5 \times 10^3$, maximum injection time of 25 ms, isolation window of m/z

2 and NCE of 30%. Dynamic exclusion of 30 s was enabled. Data was searched by MaxQuant 1.4 against the UniProt homo sapien protein database. Trypsin was selected as enzyme. LFQ quantification and match between run were enabled and all other settings were default. The data sets (dsRNA, ZIKV, LCMV and respective controls) were imported into Perseus software (version 1.6.12.0). Label-free quantification (LFQ)/ or MS2 values were log2 transformed. Reverse database hits, potential contaminants, proteins only identified by site (a peptide carrying a modified residue), and proteins with 1 or less unique/razor peptides were removed from the matrices prior to t test statistical analysis. The permutation FDR corrected p- value less than 0.05 alongside a minimum of 3-5 measurements per group required for significance allowed identification of significantly upregulated or downregulated proteins following stimulation/infection of dsRNA, ZIKV or LCMV, and their respective controls. The transformed and filtered data was exported into the web-based software VolcanoseR, to visualise significantly changed proteins with a criterion of having a log2 fold change $< -2$ or $> 2$ and an FDR corrected P-value $< 0.05$. Hierarchical clustering was performed across all replicates and was visualised via the "ComplexHeatmap" package. Functional enrichment analysis was performed on significantly enriched proteins via the R package "Clusterprofiler" and visualised using "enrichplot" in the form of a tree-plot. The t test significant protein lists from each condition were visualised via their interactions using the STRING (Search Tool for the Retrieval of Interacting Genes/Proteins) database. The interaction data from STRING can be enhanced and adapted in cytoscape to produce enhanced network visualisation. Clustering of the network was performed using ClusterONE (Clustering with Overlapping Neighbourhood Expansion) with a p-value $< 0.05$ cut-off.

**Quantitative lipidomics**

Samples were analysed by ultrahigh performance liquid chromatography (UHPLC) coupled to tandem mass spectrometry (MS/MS) employing a Vanquish UHPLC coupled to an Orbitrap Fusion Lumos mass spectrometer (Thermo Fisher Scientific, San Jose, CA, USA), with separate runs in positive and negative ion polarities. Solvent A was 6/4 (v/v) acetonitrile/water with 5 mM medronic acid and solvent B was 9/1 (v/v) isopropanol/acetonitrile. Both solvents A and B contained 10 mM ammonium acetate. 10 µl of each sample was injected into an Acquity UPLC HSS T3 C18 column (1 x 150 mm, 1.8 µm: Waters, Milford, MA, USA) at 50 °C at a flow rate of 60 µL/min for 3 min using 3% solvent B. During separation, the percentage of solvent B was increased from 3% to 70% in 5 min and from 70% to 99% in 16 min. Subsequently, the percentage of solvent B was maintained at 99% for 3 min. Finally, the percentage of solvent B was decreased to 3% in 0.1 min and maintained for 3.9 min. All MS experiments were performed using an electrospray ionization source. The spray voltages were 3.5 kV in positive ionisation-mode and 3.0 kV in negative ionisation-mode. In both polarities, the flow rates of sheath, auxiliary and sweep gases were 25 and 5 and 0 arbitrary unit(s), respectively. The ion transfer tube and vaporizer temperatures were maintained at 300 °C and 150 °C, respectively, and the ion funnel RF level was set at 50%. In the positive ionisation-mode from 3 to 24 min, top speed data-dependent scan with a cycle time of 1 s was used. Within each cycle, a full-scan MS-spectra were acquired firstly in the Orbitrap at a mass resolving power of 120,000 (at m/z 200) across an m/z range of 300–2000 using quadrupole isolation, an automatic gain control (AGC) target of 4e5 and a maximum injection time of 50 milliseconds, followed by higher-energy collisional dissociation (HCD)-MS/MS at a mass resolving power of 15,000 (at m/z 200), a normalised collision energy (NCE) of 27% at positive mode and 30% at negative mode, an m/z isolation window of 1, a maximum injection time of 35 milliseconds and an AGC target of 5e4. For the improved structural characterisation of glycerophosphocholine (PC) lipid cations, a data-dependent product ion (m/z 184.0733)-triggered

collision-induced dissociation (CID)-MS/MS scan was performed in the cycle using a q-value of 0.25 and a NCE of 30%, with other settings being the same as that for HCD-MS/MS. For the improved structural characterisation of triacylglycerol (TG) lipid cations, the fatty acid + NH3 neutral loss product ions observed by HCD-MS/MS were used to trigger the acquisition of the top-3 data-dependent ion trap CID-MS3 scans in the cycle using a q-value of 0.25 and a NCE of 30%, with other settings being the same as that for HCD-MS/MS. Dynamic exclusion of 15 s was enabled and only ions with charge state of 1-3 were selected for fragmentation.

**Lipid Identification and functional annotation analyses**

LC-MS/MS data was searched through MS Dial 4.90. The mass accuracy settings are 0.005 Da and 0.025 Da for MS1 and MS2. The minimum peak height is 50000 and mass slice width is 0.05 Da. The identification score cut off is 80%. Post identification was done with a text file containing name and m/z of each standard in SPLASH® LIPIDOMIX® Mass Spec Standard (Cat. 330707, Avanti Polar Lipids, Birmingham, AL, USA). In positive mode, [M+H]+, [M+NH4]+ and [M+H-H2O]+ were selected as ion forms. In negative mode, [M-H]- and [M+CH3COO]- were selected as ion forms. All lipid classes available were selected for the search. PC, LPC, DG, TG, CE, SM were identified and quantified at positive mode while PE, LPE, PS, LPS, PG, LPG, PI, LPI, PA, LPA, Cer, CL were identified and quantified at negative mode. The retention time tolerance for alignment is 0.1 min. Lipids with maximum intensity less than 5-fold of average intensity in blank was removed. All other settings were default. All lipid LC-MS features were manually inspected and re-integrated when needed. These four types of lipids, 1) lipids with only sum composition except SM, 2) lipid identification due to peak tailing, 3) retention time outliner within each lipid class, 4) LPA and PA artifacts generated by in-source fragmentation of LPS and PS were also removed. The shorthand notation used for lipid classification and structural representation follows the nomenclature proposed previously (*66*). Quantification of lipid species in the unit of pmol from each sample was achieved by comparison of the LC peak areas of identified lipids against those of the corresponding internal lipid standards in the same lipid class and the quantity of each lipid standard at pmol. Since the lipid class of analyte and internal standard are identical but no co-ionization of analyte and IS are achieved, it's categorized as level 3 quantification by Lipidomics Standards Initiative (lipidomicstandards.org/). Finally, the lipid species at the class, subclass or molecular species levels were normalized to either the total lipid concentration (i.e., mol% total lipid), or total lipid-class concentration (i.e., mol% total lipid class). For the lipid classes without correspondent stable isotope-labelled lipid standards, the LC peak areas of individual molecular species within these classes were normalised as follows: the MG species against the DG (18:1D7_15:0); the LPG against the PG (18:1D7_15:0), the LPA against the PA (18:1D7_15:0) and the LPS against the PS (18:1D7_15:0). All lipidomic data was imported to Excel for normalization and further processing. Significant differences between relative abundance of individual lipid species in two sample groups was acquired using unpaired two-tailed students t test (n= 3; biological replicates). Stack bar charts comparing relative abundance of major lipid categories and classes were made using Prism Version 8.4.3 software. Bubble plots of log2 fold changes in relative abundance of individual lipid species were made using R packages “ggplot2”. Relative quantification of fatty acids chain length among all 491 identified lipid species was analysed and plotted using R packages “Heatmap” and relative intensities were compared based on z-score. Principal component analysis (PCA) was performed using built in R packages (“stats”, “prcomp()”, “t”, “tibble”).

**Preparation of Artificial Lipid Droplets (aLDs)**

Artificial lipid droplets (aLDs) were prepared based on previously published protocols (*36*). A total of 1.3 mg of phospholipids including DOPC (1,2-dioleoyl-sn-glycero-3-phosphocholine), DOPE (1,2-dioleoyl-sn-glycero-3 phosphoethanolamine) and l-α-phosphatidylinositol (Soy PI) (sodium salt), dissolved in chloroform at 32 mM, were transferred to a 1.5 mL microcentrifuge and mixed in a molar ratio of 9:3:1, respectively (MERK-Avanti Polar Lipids). ATTO ATTO 647 N PPE (ATTO-TEC GmbH), a fluorescence membrane probe, was added to the lipid mixture at a final concentration of 1 mM. The mixture was then dried under a stream of N2 followed by hydrating the dried phospholipid film by addition of 100 µL of prewarmed Buffer B (20 mM HEPES, 100 mM KCl, 2 mM MgCl2, pH 7.4) incubated at 37 °C for 1 min. This was followed by the addition of 5 mg TAG (triglycerides; Triolein- MERK-Avanti Polar Lipids) and vortexed for 24 cycles of 10 s on and 10 s off to reach a crude emulsion. The emulsion was centrifuged at 1,000 × g for 5 mins at RT, and the infranatant was collected. Individual fatty acids were added to the phospholipid mixture at 2% of the total amount of lipids (0.4 mol). The fatty acids used in this study include Arachidonic Acid (5 mg/ml, CAT#181198, Sigma Aldrich), cis-5,8,11,14,17-Eicosapentaenoic acid (50 mg/ml, CAT# E2011, Sigma Aldrich), cis-4,7,10,13,16,19-Docosahexaenoic acid (50 mg/ml, CAT#D2534, Sigma Aldrich), all-cis-7,10,13,16,19-Docosapentaenoic acid (50 mM, CAT#D1797, Sigma Aldrich), Lignoceric acid (30 mg/ml, CAT# L6641, Sigma Aldrich), Nervonic acid (30 mg/ml, CAT#N1514, Sigma Aldrich), Heptacosanoic Acid (50mM, AMBH97BA00FA, Ambeed, Inc.), Tricosanoic acid (590 mM, CAT# T6543, Sigma Aldrich). The size distribution and particle concentration of aLDs was quantified using the ZetaView® system (Particle Metrix—ZetaView®, Inning am Ammersee, Germany). Morphology and general General characteristics and morphology were assessed using fluorescence microscopy on a Nikon T*i*E microscope at 60× magnification.

**Computational Modelling**

The cryo-EM structure of a viral RNA mimetic in complex with RIG-1 (PDB code: 7TNY, ) was manually docked onto a POPC lipid bilayer (to mimic a LD) created using the simulations setup module in Maestro (Schrodinger L.L.C). The interface of RIG-I was chosen based upon bioinformatics predictions (DisoLipPred) which highlighted amino acids 783-790 (IQTHEKFI) within the HEL2 domain as hypothetical binders of lipids. The protein-lipid-RNA system was then prepared using the Protein Preparation Wizard (Schrodinger L.L.C) to assign bond orders, add hydrogens, optimise hydrogen bonding networks, and minimise the structure with the OPLS4 force field. The complex was then solvated in an orthorhombic box using the TIP3P water model, with a buffer distance of 10 Å from the solute. $Na^+$ and $Cl^-$ ions were added to neutralise the system and mimic a physiological salt concentration (0.15 M). A 10-nanosecond molecular dynamics (MD) simulation was then performed using the Desmond simulation package (Schrödinger, LLC) with trajectory snapshots were saved every 100 ps for analysis. Figures were created using The PyMOL Molecular Graphics System, Version 3.0 Schrödinger, LLC.

**Statistical Analysis and Reproducibility**

Student's t tests were used for statistical analysis between 2 groups, with experiments with 2 or more experimental groups statistically analysed using either an ordinary one, or two-way multiple comparison ANOVA or multiple t tests using the Holm-Sidak method for corrections for multiple comparisons with $P< 0.05$ considered to be significant. Omics data was analysed and plotted using R packages Version 4.3.0 as stated in relevant sections. All statistical analysis (unless otherwise indicated) was performed using Prism Version 8.4.3 software (GraphPad, La Jolla, United States). All experiments were performed in biological triplicate (unless otherwise stated), and technical

duplicates were also performed for RT-PCRs. Error bars represent mean ± SEM, with a P value less than 0.05 considered to be significant. * P<0.05, ** P<0.01, *** P<0.001, **** P<0.0001.

# References


1. K. M. Crosse, E. A. Monson, A. B. Dumbrepatil, Viperin binds STING and enhances the type-I interferon response following dsDNA detection. *Immunol. Cell Biol.*

2. A. B. Dumbrepatil, S. Ghosh, K. A. Zegalia, P. A. Malec, J. D. Hoff, R. T. Kennedy, E. N. G. Marsh, Viperin interacts with the kinase IRAK1 and the E3 ubiquitin ligase TRAF6, coupling innate immune signaling to antiviral ribonucleotide synthesis. *J. Biol. Chem.* **294**, 6888–6898 (2019).

3. E. L. Arrese, F. Z. Saudale, J. L. Soulages, Lipid Droplets as Signaling Platforms Linking Metabolic and Cellular Functions. *Lipid Insights* **7**, 7–16 (2014).

4. R. Dhiman, S. Caesar, A. R. Thiam, B. Schrul, Mechanisms of protein targeting to lipid droplets: A unified cell biological and biophysical perspective. *Semin. Cell Dev. Biol.*, doi: 10.1016/j.semcdb.2020.03.004 (2020).

5. A. R. Thiam, M. Beller, The why, when and how of lipid droplet diversity. *J. Cell Sci.* **130**, 315–324 (2017).

6. J. A. Olzmann, P. Carvalho, Dynamics and functions of lipid droplets. *Nat. Rev. Mol. Cell Biol.* **20**, 137–155 (2019).

7. G. Onal, O. Kutlu, D. Gozuacik, S. Dokmeci Emre, Lipid Droplets in Health and Disease. *Lipids Health Dis.* **16**, 128 (2017).

8. E. A. Monson, A. M. Trenerry, J. L. Laws, J. M. Mackenzie, K. J. Helbig, Lipid droplets and lipid mediators in viral infection and immunity. *FEMS Microbiol. Rev.*, doi: 10.1093/femsre/fuaa066 (2021).

9. A. Zadoorian, X. Du, H. Yang, Lipid droplet biogenesis and functions in health and disease. *Nat. Rev. Endocrinol.* **19**, 443–459 (2023).

10. E. A. Monson, K. M. Crosse, M. Duan, W. Chen, R. D. O'Shea, L. M. Wakim, J. M. Carr, D. R. Whelan, K. J. Helbig, Intracellular lipid droplet accumulation occurs early following viral infection and is required for an efficient interferon response. *Nat. Commun.* **12**, 4303 (2021).

11. M. Bosch, M. Sánchez-Álvarez, A. Fajardo, R. Kapetanovic, B. Steiner, F. Dutra, L. Moreira, J. A. López, R. Campo, M. Marí, F. Morales-Paytuví, O. Tort, A. Gubern, R. M. Templin, J. E. B. Curson, N. Martel, C. Català, F. Lozano, F. Tebar, C. Enrich, J. Vázquez, M. A. Del Pozo, M. J. Sweet, P. T. Bozza, S. P. Gross, R. G. Parton, A. Pol, Mammalian lipid droplets are innate immune hubs integrating cell metabolism and host defense. *Science* **370** (2020).

12. K. Rösch, M. Kwiatkowski, S. Hofmann, A. Schöbel, C. Grüttner, M. Wurlitzer, H. Schlüter, E. Herker, Quantitative Lipid Droplet Proteome Analysis Identifies Annexin A3 as a Cofactor for HCV Particle Production. *Cell Rep.* **16**, 3219–3231 (2016).

13. E. Dixit, S. Boulant, Y. Zhang, A. S. Y. Lee, C. Odendall, B. Shum, N. Hacohen, Z. J. Chen, S. P. Whelan, M. Fransen, M. L. Nibert, G. Superti-Furga, J. C. Kagan, Peroxisomes are signaling platforms for antiviral innate immunity. *Cell* **141**, 668–681 (2010).

14. O. Khantisitthiporn, B. Shue, N. S. Eyre, C. W. Nash, L. Turnbull, C. B. Whitchurch, K. H. Van der Hoek, K. J. Helbig, M. R. Beard, Viperin interacts with PEX19 to mediate peroxisomal augmentation of the innate antiviral response. *Life Sci. Alliance* **4**, e202000915 (2021).

15. M. Du, Z. J. Chen, DNA-induced liquid phase condensation of cGAS activates innate immune signaling. *Science* **361**, 704–709 (2018).

16. R. Álvarez, D. J. López, J. Casas, V. Lladó, M. Higuera, T. Nagy, M. Barceló, X. Busquets, P. V. Escribá, G protein-membrane interactions I: Gαi1 myristoyl and palmitoyl modifications in protein-lipid interactions and its implications in membrane microdomain localization. *Biochim. Biophys. Acta* **1851**, 1511–1520 (2015).

17. E. Yamamoto, T. Akimoto, A. C. Kalli, K. Yasuoka, M. S. P. Sansom, Dynamic interactions between a membrane binding protein and lipids induce fluctuating diffusivity. *Sci. Adv.* **3**, e1601871 (2017).

18. W. Cho, R. V. Stahelin, Membrane-protein interactions in cell signaling and membrane trafficking. *Annu. Rev. Biophys. Biomol. Struct.* **34**, 119–151 (2005).

19. D. Casares, P. V. Escribá, C. A. Rosselló, Membrane Lipid Composition: Effect on Membrane and Organelle Structure, Function and Compartmentalization and Therapeutic Avenues. *Int. J. Mol. Sci.* **20** (2019).

20. A. G. York, K. J. Williams, J. P. Argus, Q. D. Zhou, G. Brar, L. Vergnes, E. E. Gray, A. Zhen, N. C. Wu, D. H. Yamada, C. R. Cunningham, E. J. Tarling, M. Q. Wilks, D. Casero, D. H. Gray, A. K. Yu, E. S. Wang, D. G. Brooks, R. Sun, S. G. Kitchen, T.-T. Wu, K. Reue, D. B. Stetson, S. J. Bensinger, Limiting Cholesterol Biosynthetic Flux Spontaneously Engages Type I IFN Signaling. *Cell* **163**, 1716–1729 (2015).

21. M. J. Hofer, W. Li, P. Manders, R. Terry, S. L. Lim, N. J. C. King, I. L. Campbell, Mice deficient in STAT1 but not STAT2 or IRF9 develop a lethal CD4+ T-cell-mediated disease following infection with lymphocytic choriomeningitis virus. *J. Virol.* **86**, 6932–6946 (2012).

22. D. J. Bonthius, B. Nichols, H. Harb, J. Mahoney, B. Karacay, Lymphocytic choriomeningitis virus infection of the developing brain: critical role of host age. *Ann. Neurol.* **62**, 356–374 (2007).

23. R. Lindqvist, F. Mundt, J. D. Gilthorpe, S. Wölfel, N. O. Gekara, A. Kröger, A. K. Överby, Fast type I interferon response protects astrocytes from flavivirus infection and virus-induced cytopathic effects. *J. Neuroinflammation* **13**, 277 (2016).

24. C. Pfefferkorn, C. Kallfass, S. Lienenklaus, J. Spanier, U. Kalinke, M. Rieder, K.-K. Conzelmann, T. Michiels, P. Staeheli, Abortively infected astrocytes appear to represent the main source of interferon beta in the virus-infected brain. *J. Virol.* **90**, 2031–2038 (2016).

25. H. Kambara, F. Niazi, L. Kostadinova, D. K. Moonka, C. T. Siegel, A. B. Post, E. Carnero, M. Barriocanal, P. Fortes, D. D. Anthony, S. Valadkhan, Negative regulation of the interferon response by an interferon-induced long non-coding RNA. *Nucleic Acids Res.* **42**, 10668–10680 (2014).

26. N. Au-Yeung, R. Mandhana, C. M. Horvath, Transcriptional regulation by STAT1 and STAT2 in the interferon JAK-STAT pathway. *JAKSTAT* **2**, e23931 (2013).

27. J. L. Jacobs, C. B. Coyne, Mechanisms of MAVS regulation at the mitochondrial membrane. *J. Mol. Biol.* **425**, 5009–5019 (2013).

28. A. Katuwawala, B. Zhao, L. Kurgan, DisoLipPred: accurate prediction of disordered lipid-binding residues in protein sequences with deep recurrent networks and transfer learning. *Bioinformatics* **38**, 115–124 (2021).

29. W. Wang, A. M. Pyle, The RIG-I receptor adopts two different conformations for distinguishing host from viral RNA ligands. *Mol. Cell* **82**, 4131-4144.e6 (2022).

30. K. Onomoto, K. Onoguchi, M. Yoneyama, Regulation of RIG-I-like receptor-mediated signaling: interaction between host and viral factors. *Cell. Mol. Immunol.* **18**, 539–555 (2021).

31. B. Omasta, J. Tomaskova, Cellular lipids-hijacked victims of viruses. *Viruses* **14**, 1896 (2022).

32. M. Papin, A. M. Bouchet, A. Chantôme, C. Vandier, Ether-lipids and cellular signaling: A differential role of alkyl- and alkenyl-ether-lipids? *Biochimie* **215**, 50–59 (2023).

33. Y. Feng, S. Qiu, S. Zou, R. Li, H. Chen, K. Chen, J. Ma, J. Liu, X. Lai, S. Liu, M. Zou, Antiviral activity of eicosapentaenoic acid against zika virus and other enveloped viruses. *Front. Pharmacol.* **16**, 1564504 (2025).

34. X. Suo, J. Wang, D. Wang, G. Fan, M. Zhu, B. Fan, X. Yang, B. Li, DHA and EPA inhibit porcine coronavirus replication by alleviating ER stress. *J. Virol.*, e0120923 (2023).

35. C.-Y. Chang, C.-C. Wu, J.-D. Wang, J.-R. Li, Y.-Y. Wang, S.-Y. Lin, W.-Y. Chen, S.-L. Liao, C.-J. Chen, DHA attenuated Japanese Encephalitis virus infection-induced neuroinflammation and neuronal cell death in cultured rat Neuron/glia. *Brain Behav. Immun.* **93**, 194–205 (2021).

36. Z. Telikani, I. Amarasinghe, V. Impicciche, A. Nalbantlar, J. Whan, K. Caracciolo, J. I. Phillips, J. L. Dutton, L. A. Wallace, A. Jamal, T. A. Gibson Hughes, K. S. Okuda, A. Mechler, E. A. Monson, K. J. Helbig, The phospholipid composition of artificial lipid droplets enhances their deliverability and facilitates a broad Biodistribution in vivo and in vitro. *Acta Biomater.*, doi: 10.1016/j.actbio.2025.05.002 (2025).

37. S. E. Farley, J. E. Kyle, H. C. Leier, L. M. Bramer, J. B. Weinstein, T. A. Bates, J.-Y. Lee, T. O. Metz, C. Schultz, F. G. Tafesse, A global lipid map reveals host dependency factors conserved across SARS-CoV-2 variants. *Nat. Commun.* **13**, 3487 (2022).

38. Q. Chen, J. Gouilly, Y. J. Ferrat, A. Espino, Q. Glaziou, G. Cartron, H. El Costa, R. Al-Daccak, N. Jabrane-Ferrat, Metabolic reprogramming by Zika virus provokes inflammation in human placenta. *Nat. Commun.* **11**, 2967 (2020).

39. H. C. Leier, J. B. Weinstein, J. E. Kyle, J.-Y. Lee, L. M. Bramer, K. G. Stratton, D. Kempthorne, A. R. Navratil, E. G. Tafesse, T. Hornemann, W. B. Messer, E. A. Dennis, T. O. Metz, E. Barklis, F. G. Tafesse, A global lipid map defines a network essential for Zika virus replication. *Nat. Commun.* **11**, 3652 (2020).

40. J. Hehner, L. Schneider, A. Woitalla, B. Ott, K. C. T. Vu, A. Schöbel, T. Hain, D. Schwudke, E. Herker, Glycerophospholipid remodeling is critical for orthoflavivirus infection. *Nat. Commun.* **15**, 8683 (2024).

41. D. Poddar, N. Sharma, T. Ogino, X. Qi, P. M. Kessler, H. Mendries, R. Dutta, G. C. Sen, The interferon-induced protein, IFIT2, requires RNA-binding activity and neuronal expression to protect mice from intranasal vesicular stomatitis virus infection. *MBio* **15**, e0056824 (2024).

42. G. I. Vladimer, M. W. Górna, G. Superti-Furga, IFITs: Emerging roles as key anti-viral proteins. *Front. Immunol.* **5**, 94 (2014).

43. A. Pichlmair, C. Lassnig, C.-A. Eberle, M. W. Górna, C. L. Baumann, T. R. Burkard, T. Bürckstümmer, A. Stefanovic, S. Krieger, K. L. Bennett, T. Rülicke, F. Weber, J. Colinge, M. Müller, G. Superti-Furga, IFIT1 is an antiviral protein that recognizes 5’-triphosphate RNA. *Nat. Immunol.* **12**, 624–630 (2011).

44. K. M. Crosse, E. A. Monson, A. B. Dumbrepatil, M. Smith, Y.-Y. Tseng, K. H. Van der Hoek, P. A. Revill, S. Saker, D. C. Tscharke, E. N. G Marsh, M. R. Beard, K. J. Helbig, Viperin binds STING and enhances the type-I interferon response following dsDNA detection. *Immunol. Cell Biol.*, doi: 10.1111/imcb.12420 (2020).

45. T. Saitoh, T. Satoh, N. Yamamoto, S. Uematsu, O. Takeuchi, T. Kawai, S. Akira, Antiviral protein Viperin promotes Toll-like receptor 7- and Toll-like receptor 9-mediated type I interferon production in plasmacytoid dendritic cells. *Immunity* **34**, 352–363 (2011).

46. K.-R. Chen, C.-Y. Yang, S.-G. Shu, Y.-C. Lo, K.-W. Lee, L.-C. Wang, J.-B. Chen, M.-C. Shih, H.-C. Chang, Y.-J. Hsiao, C.-L. Wu, T.-H. Tan, P. Ling, Endosomes serve as signaling platforms for RIG-I ubiquitination and activation. *Sci. Adv.* **10**, eadq0660 (2024).

47. H. Ishikawa, G. N. Barber, STING is an endoplasmic reticulum adaptor that facilitates innate immune signalling. *Nature* **455**, 674–678 (2008).

48. M. Pöhnl, M. F. W. Trollmann, R. A. Böckmann, Nonuniversal impact of cholesterol on membranes mobility, curvature sensing and elasticity. *Nat. Commun.* **14**, 8038 (2023).

49. H. Sunshine, M. L. Iruela-Arispe, Membrane lipids and cell signaling. *Curr. Opin. Lipidol.* **28**, 408–413 (2017).

50. M. F. Brown, Curvature forces in membrane lipid-protein interactions. *Biochemistry* **51**, 9782–9795 (2012).

51. J. N. Israelachvili, D. J. Mitchell, B. W. Ninham, Theory of self-assembly of hydrocarbon amphiphiles into micelles and bilayers. *J. Chem. Soc.* **72**, 1525 (1976).

52. A. Grabon, V. A. Bankaitis, M. I. McDermott, The interface between phosphatidylinositol transfer protein function and phosphoinositide signaling in higher eukaryotes. *J. Lipid Res.* **60**, 242–268 (2019).

53. X. Ma, Z. Zhi, S. Zhang, C. Zhou, A. Mechler, P. Liu, Validating an artificial organelle: Studies of lipid droplet-specific proteins on adiposome platform. *iScience* **24**, 102834 (2021).

54. J. C. Bozelli Jr, W. Jennings, S. Black, Y. H. Hou, D. Lameire, P. Chatha, T. Kimura, B. Berno, A. Khondker, M. C. Rheinstädter, R. M. Epand, Membrane curvature allosterically regulates the phosphatidylinositol cycle, controlling its rate and acyl-chain composition of its lipid intermediates. *J. Biol. Chem.* **293**, 17780–17791 (2018).

55. J. M. Dean, I. J. Lodhi, Structural and functional roles of ether lipids. *Protein Cell* **9**, 196–206 (2018).

56. A. Kohn, J. Gitelman, M. Inbar, Interaction of polyunsaturated fatty acids with animal cells and enveloped viruses. *Antimicrob. Agents Chemother.* **18**, 962–968 (1980).

57. A. Goc, A. Niedzwiecki, M. Rath, Polyunsaturated ω-3 fatty acids inhibit ACE2-controlled SARS-CoV-2 binding and cellular entry. *Sci. Rep.* **11**, 5207 (2021).

58. M.-J. Olarte, J. M. J. Swanson, T. C. Walther, R. V. Farese Jr, The CYTOLD and ERTOLD pathways for lipid droplet-protein targeting. *Trends Biochem. Sci.* **47**, 39–51 (2022).

59. I. Amarasinghe, W. Phillips, A. F. Hill, L. Cheng, K. J. Helbig, E. Willms, E. A. Monson, Cellular communication through extracellular vesicles and lipid droplets. *J. Extracell. Biol.* **2** (2023).

60. H. Vitrac, D. M. MacLean, V. Jayaraman, M. Bogdanov, W. Dowhan, Dynamic membrane protein topological switching upon changes in phospholipid environment. *Proc. Natl. Acad. Sci. U. S. A.* **112**, 13874–13879 (2015).

61. A. E. F. Sheppe, M. J. Edelmann, Roles of eicosanoids in regulating inflammation and neutrophil migration as an innate host response to bacterial infections. *Infect. Immun.* **89**, e0009521 (2021).

62. K. J. Helbig, J. M. Carr, J. K. Calvert, S. Wati, J. N. Clarke, N. S. Eyre, S. K. Narayana, G. N. Fiches, E. M. McCartney, M. R. Beard, Viperin is induced following dengue virus type-2 (DENV-2) infection and has anti-viral actions requiring the C-terminal end of viperin. *PLoS Negl. Trop. Dis.* **7**, e2178 (2013).

63. X. Zhou, B. B. Moore, Lung Section Staining and Microscopy. *Bio Protoc* **7** (2017).

64. D. R. Whelan, T. Holm, M. Sauer, T. D. M. Bell, Focus on super-resolution imaging with direct Stochastic Optical Reconstruction Microscopy (dSTORM). *Aust. J. Chem.* **67**, 179 (2014).

65. J. Folch, M. Lees, G. H. Sloane Stanley, A simple method for the isolation and purification of total lipides from animal tissues. *J. Biol. Chem.* **226**, 497–509 (1957).

66. G. Liebisch, E. Fahy, J. Aoki, E. A. Dennis, T. Durand, C. S. Ejsing, M. Fedorova, I. Feussner, W. J. Griffiths, H. Köfeler, A. H. Merrill Jr, R. C. Murphy, V. B. O'Donnell, O. Oskolkova, S. Subramaniam, M. J. O. Wakelam, F. Spener, Update on LIPID MAPS classification, nomenclature, and shorthand notation for MS-derived lipid structures. *J. Lipid Res.* **61**, 1539–1555 (2020).

## Supplementary Files

This is a list of supplementary files associated with this preprint. Click to download.

- SuplementaryTableS2dsRNALDproteomeOntology.pdf
- SuplementaryTableS3ZIKVLDproteome.pdf
- SuplementaryTableS4lipidome.pdf
- SuplementaryTableS1LCMVLDproteome.pdf
- Movie2.mp4
- SupplimentaryMaterials.docx
- Movie4.mp4
- Movie1.mp4
- Movie3.mp4